Altered Cortical Ensembles in Mouse Models of Schizophrenia

Highlights

- Neuronal ensemble activity is less reliable in mouse chronic ketamine model

- Ensembles are affected in mouse genetic model of schizophrenia

- Abnormal ensembles are found in both spontaneous and sensory-evoked activity

- Data are consistent with schizophrenia being a disease of cortical attractors

Authors

Jordan P. Hamm, Darcy S. Peterka, Joseph A. Gogos, Rafael Yuste

Correspondence

jph2164@columbia.edu

In Brief

Hamm et al. studied sensory cortical populations in two established mouse models of schizophrenia pathophysiology and risk, chronic ketamine and $Df(16)A^{+/-}$. They identify a disorganization of neuronal ensembles, distinct from alterations in neuronal or global activity levels or pairwise correlations, that could constitute the common pathophysiology of the disease.

CrossMark

CellPress

Article

Altered Cortical Ensembles in Mouse Models of Schizophrenia

Jordan P. Hamm,[1,4,*] Darcy S. Peterka,[1] Joseph A. Gogos,[2,3] and Rafael Yuste[1,3]

[1]Neurotechnology Center, Department of Biological Sciences, Columbia University, New York, NY 10027, USA
[2]Department of Physiology and Cellular Biophysics
[3]Department of Neuroscience
Columbia University, New York, NY 10032, USA
[4]Lead Contact
*Correspondence: jph2164@columbia.edu
http://dx.doi.org/10.1016/j.neuron.2017.03.019

SUMMARY

In schizophrenia, brain-wide alterations have been identified at the molecular and cellular levels, yet how these phenomena affect cortical circuit activity remains unclear. We studied two mouse models of schizophrenia-relevant disease processes: chronic ketamine (KET) administration and *Df(16)A*[+/−], modeling 22q11.2 microdeletions, a genetic variant highly penetrant for schizophrenia. Local field potential recordings in visual cortex confirmed gamma-band abnormalities similar to patient studies. Two-photon calcium imaging of local cortical populations revealed in both models a deficit in the reliability of neuronal coactivity patterns (ensembles), which was not a simple consequence of altered single-neuron activity. This effect was present in ongoing and sensory-evoked activity and was not replicated by acute ketamine administration or pharmacogenetic parvalbumin-interneuron suppression. These results are consistent with the hypothesis that schizophrenia is an "attractor" disease and demonstrate that degraded neuronal ensembles are a common consequence of diverse genetic, cellular, and synaptic alterations seen in chronic schizophrenia.

INTRODUCTION

Understanding of the neurobiology of schizophrenia (SZ) has progressed considerably over the past several decades. Research in human subjects with SZ has identified altered neuromodulation, excitatory/inhibitory balance, and neurodevelopmental processes at the molecular, synaptic, and single-cell levels (Lewis, 2014; Poels et al., 2014). In parallel, altered network connectivity and functional synchrony have been described in SZ at the whole-brain level (Uhlhaas and Singer, 2010; Yang et al., 2014). However, these alterations have not been connected into a coherent pathophysiology, and the heterogeneity and non-specificity of these biomarkers within and across multiple psychiatric diagnostic groups have complicated attempts (Clementz et al., 2016).

Perhaps at the heart of this issue is the possibility that the fundamental neural deviations that set SZ apart from other neuropsychiatric syndromes are best understood not at elemental (proteins and single neuron) or global levels (gross anatomy and fMRI), but at the circuit level (Arguello and Gogos, 2012; Sigurdsson et al., 2010) and within the stable dynamics of intricately connected, local neocortical populations (Rolls et al., 2008; Wang and Krystal, 2014). For instance, recent work in rodents has shown that local populations of neurons in both sensory and association regions exhibit repeating patterns of activity made up of multineuronal "ensembles," coactive groups of neurons (Hebb, 1949) that are conserved across brain states and stimulation paradigms (Carrillo-Reid et al., 2015, 2016; Harvey et al., 2012; Luczak et al., 2009; Miller et al., 2014). These observations support the hypothesis that neural circuits have evolved to build emergent functional states, such as "attractors," consisting of stable or semistable, recurrent activity patterns that would theoretically underlie thoughts, perception, and action (Hopfield, 1982; Yuste, 2015).

It is therefore plausible that in SZ, a diversity of lower-level molecular or synaptic alterations could generate a systematic disorganization of local cortical ensembles, effectively destabilizing otherwise reliable activity patterns present within neocortical networks. In fact, in SZ patients, alterations in the functional dynamics of global networks have been inferred from changes in interregional BOLD signal correlations (fMRI) and oscillatory coherence (EEG) (Lo et al., 2015; Uhlhaas and Singer, 2010; Zhu et al., 2016), providing some evidence for a circuit pathophysiology at the macroscale. Albeit very informative, such whole-brain methods provide only gross estimations of activity within local regions of the cortex, essentially averaging across the activity of tens to hundreds of thousands of neurons in a single measurement and thus lacking the single-neuron resolution that may be critically necessary to differentiate and assess the robustness of repeating ensemble activations in local territories. Indeed, a degradation of consistent synchrony among local ensembles could undermine the robustness of signaling within larger brain networks and underlie macro-level network abnormalities. At the behavioral level, spontaneously active and inconsistently stimulus-driven ensembles or "attractor" patterns could explain positive symptoms (perceptual distortions, hallucinations, and loose associations), while internally driven patterns, which are unstable and highly susceptible to distraction, could account for cognitive deficits (Rolls et al., 2008).

Though theoretically powerful, empirical evidence for this pathophysiological framework at the circuit local level is lacking. To directly study the multineuronal dynamics of cortical microcircuits, we performed two-photon calcium imaging (2P-Ca^{2+}), a method enabling stable, long-term observation of single-cell spiking activity and patterned coactivations (ensemble activations) across local populations of neurons simultaneously in awake mice (Cossart et al., 2003; Stosiek et al., 2003; Yuste and Katz, 1991). We first induced an SZ-relevant brain state in mice using the well-established ketamine (KET) pharmacological approach (Behrens et al., 2007). In humans, acute blockade of N-methyl D-aspartate glutamate receptors (NMDARs; with, e.g., KET) consistently induces positive, negative, and cognitive symptomology of SZ (Krystal et al., 1994). While neither an acute nor a chronic KET model can be said to produce SZ in mice, the chronic KET model recreates numerous SZ-relevant phenotypes at multiple functional levels (Behrens et al., 2007; Phoumthiphavong et al., 2016). Indeed, in mice, chronic (7–14 days) subanesthetic KET not only affects NMDAR neurotransmission, but recapitulates key SZ pathophysiology, including alterations in parvalbumin-containing (PV) interneurons (Behrens et al., 2007), gamma oscillations (McNally et al., 2013; Sullivan et al., 2015), dopaminergic levels and gene expression (Chatterjee et al., 2012), dendritic spines (Phoumthipphavong et al., 2016), and cognition (Featherstone et al., 2012).

In addition, we examined neocortical ensemble dynamics in a mouse model of significant genetic risk for SZ. Deletions in the 22q11.2 portion of the human chromosome result in sporadic cases of SZ in 30% of carriers, a penetrance that is among the highest of all known risk genotypes for the disease (Hiroi et al., 2013). Like other high-penetrance genetic risk factors, this mutation nevertheless accounts for a small proportion of the SZ population (approximately 1% of cases). But, importantly, individuals with SZ due to this genetic variant are phenotypically identical to the rest of the SZ population (Karayiorgou et al., 2010), sharing not only symptomology but also gray matter alterations (Jalbrzikowski et al., 2013) and functional connectivity impairments (Scariati et al., 2016). This critical section of the genome carries around 25 genes expressed in the forebrain controlling dopamine catabolism (COMT), microRNA production (DGCR8), and axonal growth (RTN4R and ZDHHC8), among others (Karayiorgou et al., 2010). Genetically engineered Df(16)A$^{+/-}$ mice carry deletions syntenic to 22q11.2 deletions and recreate a mosaic of SZ pathophysiology, including deficits in cortical parvalbumin interneurons, dendritic spine stability (Fénelon et al., 2013), and axonal branching (Mukai et al., 2015), as well as impairments in synaptic plasticity (Fénelon et al., 2013) and hippocampal-prefrontal synchrony-supported working memory (Sigurdsson et al., 2010). By comparing adult Df(16)A$^{+/-}$ mice (>P60; postnatal day 60) to their wild-type (WT) littermate controls, we examined whether and how multineuronal dynamics in sensory cortices are altered in this model of SZ risk, and how such alterations compare to the KET model.

Our study examined local circuit activity in primary visual cortex (V1). Despite traditional focus on prefrontal cortex, cell- and subcellular-level pathophysiology in psychotic disease is actually cortex-wide (Glantz and Lewis, 2000; Hashimoto et al., 2008; Uhlhaas and Singer, 2010). Moreover, visual processing abnormalities in particular are robustly reported in patients (Spencer et al., 2004; Uhlhaas and Singer, 2010) and visual perceptual disturbances are actually more common than auditory sequelae in first episode patients and prodromal individuals (Javitt, 2009). Given recent progress in understanding functional properties (Niell and Stryker, 2008) and SZ biomarkers in mouse visual cortex (Hamm and Yuste, 2016), we reasoned this cortical area, which can be rigorously studied given its sensory accessibility, could provide potent translational inroads to understanding local cortical circuit dysfunction.

We find that both models produced deficits in stimulus-elicited gamma power similar to those reported in sensory cortices of human SZ patients (Spencer et al., 2004; Uhlhaas and Singer, 2010). Increased single-neuron activity and background spectral power, a less consistent finding in SZ (Hamm et al., 2014; Moran and Hong, 2011), were only observed in KET mice. But neuronal ensembles were abnormal in both models, with a systematic disorganization wherein the presence of distinct ensembles became less pronounced and recurring ensemble activations became less reliable over time. Importantly, acute NMDAR blockade and pharmacogenetic suppression of PV interneurons (using inhibitory hM4D(i) "DREADDs"; designer receptors exclusively activated by designer drugs), both components of the chronic KET model, disinhibited neuronal activity but were incapable of recreating higher-order changes. Ensemble-level disorganization in KET and Df(16)A$^{+/-}$ was present in both ongoing and visually evoked activity, supporting the shallowed neocortical "attractor" landscape hypothesis of SZ (Rolls et al., 2008). Thus, our results show that two distinct chronic manipulations modeling key aspects of SZ risk and/or synaptic dysfunction generate changes in functional circuit ensembles rather than simple alterations in activity levels or functional connectivity, thus providing a bridge between the pathophysiology of single neurons and networks in a psychiatric disease.

RESULTS

KET and Df(16)A$^{+/-}$ Models Reproduce Electrophysiological Phenotypes of SZ

To explore potentially altered dynamics of cortical circuits in the pathophysiology of SZ, we used mice treated with chronic KET or Df(16)A$^{+/-}$ mutants and performed all measurements in awake animals. Subanesthetic levels of KET (60 mg/kg/day) or an equivalent volume of saline (SAL) continuously (1 μL per hour) was administered for 1 week with a subcutaneously implanted osmotic minipump (Alzet, model 2001). Mutant Df(16)A$^{+/-}$ mice were generated as in Stark et al. (2008). We first habituated mice to awake head fixation on a rotating wheel allowing free movement and recorded local field potentials (LFPs) from layer 2/3 of V1. We focused on oscillatory activity at baseline and during the presentation of full-field grating stimuli. Frequency and time-frequency spectra were first segregated with principal component analysis (PCA) into five bins (Hamm and Yuste, 2016; Hamm et al., 2014) that conformed well to established neocortical frequency bands (Buzsaki, 2009): low/theta/alpha (1–14 Hz), beta (15–35 Hz), gamma1 (36–58 Hz), gamma2 (62–110 Hz), and high (>111 Hz).
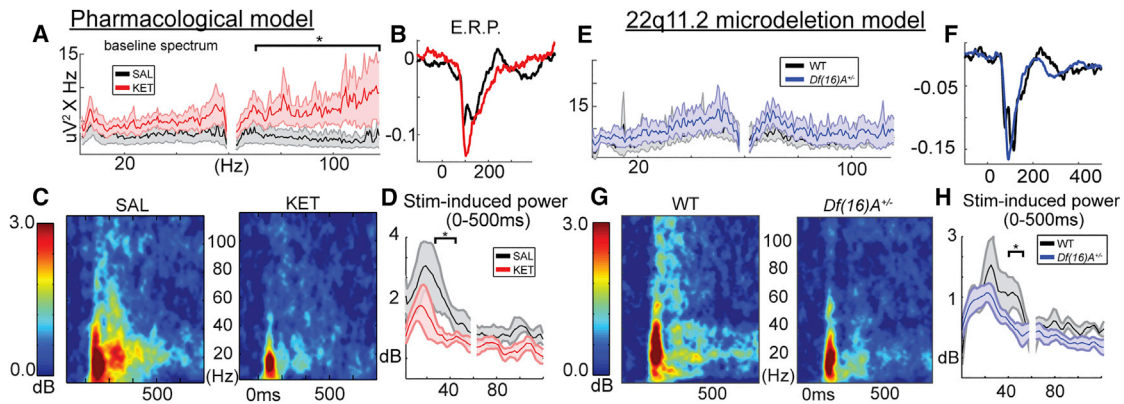
Figure 1. Abnormal Electrophysiology in KET and *Df(16)A^{+/−}* Mice

LFP recordings from mouse V1 layer 2/3.

(A) Baseline power spectra corrected for 1/f component.

(B) The waveform of the initial event-related potential (LFP averaged over trials).

(C and D) Stimulus-induced gamma power time-frequency spectra (C), averaged over the first 500 ms (D).

(E–H) Baseline spectra (E), event-related potentials (F), time frequency (G), and induced power spectra (H) plotted for *Df(16)A^{+/−}* mice versus WT (*p < 0.05, two-tailed; all spectra/lineplots averaged over all mice; $n^{sal} = 7$, $n^{ket} = 6$, $n^{df16} = 8$, $n^{control} = 5$ mice; error bars reflect SEM across mice).

Relative to SAL controls (n = 7), KET mice (n = 6) exhibited a trend-level broadband increase in baseline spectral power in the high gamma band (PCA-defined gamma2, 62–110 Hz; $t(11) = 1.81$, p = 0.09). *Df(16)A^{+/−}* (n = 8) mice, compared to their WT littermates (n = 5), did not show an increase in background spectral power at any frequency (Figures 1A and 1E; all p > 0.10; number of mice used is the same for all LFP comparisons for all conditions). But during visual stimulation a significant *decrease* in sensory-elicited gamma power was observed both in KET (first 500 ms post-stimulus onset; gamma1 [36–58 Hz], $t(11) = 2.48$, p < 0.05; gamma2, $t(11) = 2.21$, p < 0.05; Figures 1B–1D) and *Df(16)A^{+/−}* mice (gamma1, $t(11) = 2.04$, p = 0.06; gamma2, $t(11) = 3.17$, p < 0.01; Figures 1F–1H). Similar trends were observed for gamma-band inter-trial phase coherence (ITC), a measure of phase consistency of stimulus-induced oscillations (although ITC values were relatively low above 40 Hz; see Figure S1 and details in caption). Neither KET nor *Df(16)A^{+/−}* mice showed obvious alterations in arousal, as evidenced by similar locomotion rates (Figures S1E and S1F; $t^{KET}(11) = −0.12$; p < 0.90; $t^{Df16}(11) = −1.35$, p = 0.20) and similar distributions of spectral power across low (<15 Hz)- and gamma/high-frequency bands (>35 Hz; Figures 1A, 1E, S1A, and S1B; ratio, $t^{KET}(11) = −0.14$, p = 0.89; $t^{Df16}(11) = −0.25$, p = 0.81; Harris and Thiele, 2011; Vinck et al., 2015). This held true when spectra were normalized by average overall power (ostensibly; 0.5–120 Hz; Figures S1C and S1D; reflecting "relative" power). Post hoc examination of these relative power spectra demonstrated a decrease specifically at the theta peak (6.5–7 Hz) in *Df(16)A^{+/−}* ($t(11) = 2.21$, p < 0.05), but not KET, mice ($t(11) = −1.04$, p = 0.32). Alterations in prefrontal-hippocampal theta coherence have been previously reported in *Df(16)A^{+/−}* mice (Sigurdsson et al., 2010), and these effects begin to suggest that such abnormalities could extend to other neocortical regions.

Deficits in stimulus-driven gamma power are relatively consistent in patients (Brenner et al., 2009; Uhlhaas and Singer, 2010),

especially when passive, simple paradigms and large samples are studied (Hamm et al., 2014). While alterations in broadband spectral power at baseline have been reported in KET models in rodents (Kocsis et al., 2013), such increases are inconsistent across other pharmacological and genetic models of SZ (Featherstone et al., 2015; Sullivan et al., 2015), and similar observations, as well as changes in relative theta power, in SZ are present but variable (Clementz et al., 1994; Hamm et al., 2014; Hirano et al., 2015). In general, dysregulation of gamma-band dynamics and signal to noise ratio, rather than a simple increase or decrease, is a more consistent finding in SZ (Moran and Hong, 2011), and both models recapitulate this deficit in a primary sensory cortex.

KET, but Not *Df(16)A^{+/−}*, Mice Show Increased Neuronal Activity

To measure neuronal population activity with single-cell resolution, we virally expressed genetically encoded calcium indicators (GCaMP6) in layer 2/3 of left monocular V1 under the synapsin promoter, which infects neurons broadly (Figure 2), and imaged populations of 50–150 neurons from V1 in a 500 × 500 μm field of view through a surgically thinned skull (≈3.5–4.0 Hz; Figures 2A, 2B, and S2). We first focused on the spontaneous "ongoing" activity in the absence of direct stimulation (i.e., during awake rest). Multineuronal recordings have shown that non-stimulus-driven (ongoing) activity is not only abundant in sensory neocortical circuits, but shares a temporal and spatial structure with stimulus-evoked activity (Luczak et al., 2009), recapitulating an intrinsic "ensemble" vocabulary of neuronal circuits (Carrillo-Reid et al., 2015; Miller et al., 2014) and potentially supporting intrinsically generated mental states (Ji and Wilson, 2007).

Spontaneous calcium transients (putative action potential bursts; Chen et al., 2013; Smetters et al., 1999; measured by change in fluorescence, Δf/f; Figures S3, 2C, 2G, and 2K) were

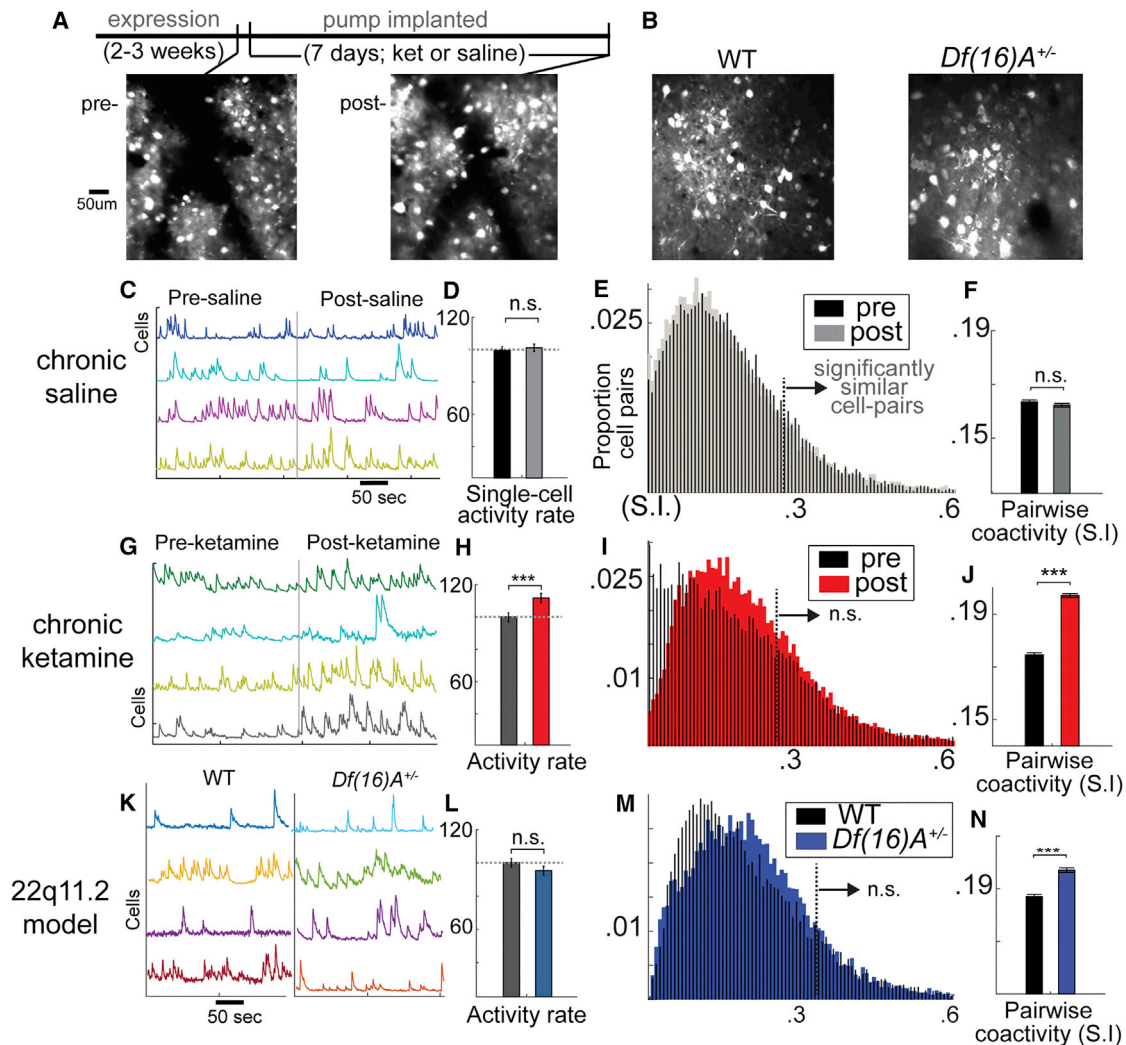**Figure 2. Abnormalities in Neuronal Activity and Correlations in KET and *Df(16)A*$^{+/-}$ Mice**

(A and B) SD projection frame of virally driven GCaMP6s expression in local V1 populations (A) before and after 1 week of minipump-delivered KET or (B) in 22q11.2 microdeletion model mice (*Df(16)A*$^{+/-}$) or WT littermate controls.

(C) Raw fluorescence traces (*f*) for single cells recorded during non-locomotive awake rest in a dark room before and after 1 week of SAL treatment.

(D) Average activity levels across cells (percent of frames showing significant increases in Δf, a signature of firing; response normalized to mouse-wise mean response pre-treatment).

(E and F) Histograms of pairwise correlated activity (similarity index), with a vertical dotted line indicating statistical cut-off for significantly correlated cell pairs (i.e., values to the right of cut-off are significant at p < 0.05) (E). Bar plot displaying average correlations over all cell pairs (F).

(G–N) Plots repeated for (G–J) chronic KET and (K–N) *Df(16)A*$^{+/-}$ (one-way ANOVA, *p < 0.05, **p < 0.01, ***p < 0.001; neuronal populations from n^{sal} = 6, n^{ket} = 6, n^{df16} = 7, n^{control} = 7 mice; error bars reflect SEM across cells/cell pairs).

quantified in active layer 2/3 neurons before and after 1 week of KET (n = 7 mice [6 for rest]; 434 cells pre-treatment [pre], 438 cells post-treatment [post]) or SAL control (n = 7 mice [6 for rest]; 436 cells pre, 443 cells post; Figure S2) or in *Df(16)A*$^{+/-}$ mice (n = 7 mice; 336 cells) or their WT littermates (n = 7 mice; 408 cells. These animal/cell counts were used for all resting-state analyses, including single-cell, pairwise, and ensemble.). When analyses focused on and were pooled across individual neurons, we found that KET increased the average Δf/f during non-locomotive rest ($F^{interaction}$(1,1716) = 3.73, p < 0.05; F^{KET}(847) = 8.17, p < 0.01; F^{SAL}(869) = 0.22, p = 0.69). This effect

became more dramatic when analyses were limited to cells measured on consecutive weeks (see Supplemental Information; Figures S4A and S4B; F^{KET}(146) = 20.61, p < 0.001), and this analysis enabled a direct comparison of absolute fluorescence values and dynamics (which vary between cells and mice due to natural [i.e., intrinsic firing rate] or artificial reasons [i.e., viral expression, skull thickness, or depth of imaging plane]). In KET mice, the frequency of calcium transients did not change ($F^{interaction}$ (1,264) = 0.77, p = 0.38), but the average size of calcium transients increased ($F^{interaction}$ (1,264) = 42.13, p < 0.001; F^{KET}(1,146) = 28.51, p < 0.001). Interestingly, relative baseline

activity levels in individual cells did not increase evenly across all neurons (pre- versus post-correlation KET, r = 0.22, p = 0.04; SAL, r = 0.52, p < 0.001; Fisher r-to-z = 2.71, p < 0.01; Figure S4C). This non-uniform increase is consistent with previous reports using acute PCP injection in rats (another NMDAR antagonist) (Kargieman et al., 2007), but as others recorded one neuron per animal, they could only infer this population-level effect.

$Df(16)A^{+/-}$ mice, on the other hand, did not show a significant change in single-neuron activity levels at rest when compared to littermate WT controls (F (1,742) = 1.66, p = 0.19; Figure 2L). These effects showed a similar pattern as analyses of background LFP spectral power, suggesting that increased gamma EEG power observed in SZ visual cortex (Venables et al., 2009) could reflect an increase in neuronal spiking in superficial neocortex. Further, KET mice in our study showed an increase in single-neuron calcium transient size, but not frequency, echoing again LFP studies in NMDAR-hypofunction mice reporting increased LFP gamma-burst magnitude, but not frequency (Carlén et al., 2012).

Disorganization of Population Activity in KET and $Df(16)A^{+/-}$ Mice

Calcium imaging in awake mice enables an examination of the functional relationships and recurrent patterns of activity present in local neuronal populations that are not accessible with LFP (Harvey et al., 2012; Miller et al., 2014). We first sought to determine whether either model showed a simple increase or decrease in coactivity among local neurons by examining the average pairwise "similarity" between all neuron pairs (i.e., estimating the proportion of shared or synchronous calcium events across time; see STAR Methods). In histograms combined across all mice and all cell pairs, both models (but not SAL) appeared to show a positive shift in the distribution toward higher similarity values (Figures 2L–2N). However, these differences were not significant: using a frame shuffling procedure (which maintained the activity level and pattern of each individual neuron), we determined that the proportion of "significantly" similar or putatively functionally correlated cell pairs (actual similarity greater than 99% of shuffled values) for each mouse/circuit was neither increased nor decreased after SAL or KET ($F^{interaction}$(1,10) = 1.92, p = 0.20), or in $Df(16)A^{+/-}$ (F (1,10) = 0.85, p = 0.37), even though average cell-cell similarity values were increased in both models ($F^{interaction}$(1,132762) = 284, p < 0.0001; F^{KET}(1,65954) = 446.4, p < 0.001; F^{SAL}(1,66812) = 1.90, p = 0.16; $F^{d(f16)A+/-}$(1,44210) = 76.0, p < 0.001; Figures 2F, 2J, and 2M).

This analysis suggested potential alterations at the ensemble or network level, but it was not clear from average pairwise synchrony alone whether and how ensembles of three or more neurons or network activity patterns are affected. For instance, when observed en masse, cortical circuits cycle between relatively quiescent periods and periods of synchronized activity (Miller et al., 2014). The latter consists of distinct groups of coactive neurons, or ensemble activations, which are neither constitutionally random nor perfectly uniform but may reflect the recurrent activity of stable "attractor" states that outline the computational building block of neuronal circuits (Carrillo-Reid et al., 2015; Hebb, 1949; Hopfield, 1982; Luczak et al., 2009; Miller et al., 2014). Thus, to comprehensively examine the effect of any manipulation on cortical circuit dynamics, one needs to measure these population-level dynamics reliably.

To do so, we first identified and defined "ensemble" activations (or high population-coactivity states) statistically for each imaging dataset as population coactivity above chance level (Figures S5A–S5C; shuffling within neurons across time). This analysis indicated that the frequency of such population-wide events was not altered in either disease model (Figures S6A–S6C). To determine if ensembles were constitutionally different in these disease models, we also characterized the instantaneous pattern of activity across all recorded neurons for each ensemble activation (i.e., which cells are active/inactive) as an n-dimensional vector (n = number of neurons). We then quantified the consistency of these states across subsequent ensemble activations using a "similarity index"; i.e., a measure of the cosine of the angle between state vectors, bound between 0 and 1 (1 = perfect similarity). Smaller angles represent highly similar vectors and, thus, points in time (or ensembles) with a highly similar constitution or distribution of local population activity (and a high similarity index).

In SAL-treated and WT animals we found, as previously reported (Miller et al., 2014), ensemble activations with similarity values far exceeding chance levels (similarity index; SI > 0.36–0.41 based on within-frame shuffling; see STAR Methods; Figures 3A, 3B, 3E, 3F, S5D, and S5E). $Df(16)A^{+/-}$ and KET mice, however, displayed a significant *decrease* in state-state similarity, as though ensemble activity was not driven by stable groups of coactive neurons but instead by continuously variable or random activity states (Figures 3C, 3D, 3G, and 3H). This was reflected in an ~35% decrease in ensemble "reactivations" across mice/circuits measured ($F^{interaction}$(1,10) = 4.98, p < 0.05; F^{KET}(1,5) = 8.01, p < 0.05; t^{SAL}(1,5) = 0.02, p = 0.90; $F^{d(f16)A+/-}$(1,12) = 6.00, p < 0.05; Figures 3I–3K). A comparison of population activity patterns pre- and post-treatment showed that while SAL mice displayed many ensembles (Figure S6D) and/or recurrent population dynamics that repeated even after 1 week (PCA; Figures S6D and S6E), KET mice largely did not (Figures S6F and S6G), suggesting that the local neuronal ensembles that are otherwise stable over time within a circuit (Carrillo-Reid et al., 2016) are disrupted in KET and $Df(16)A^{+/-}$ (Figure S6 displays data from one representative SAL mouse and one KET mouse exhibiting >40 re-identifiable neurons across weeks).

Further analyses using k-means clustering revealed that in control animals, ensemble activations appeared to consist of a small number of semi-stereotyped unique "states" (rather than one all-inclusive state; Figures 4A–4H), suggestive of distinct "basins of attraction" in the cortical network (Figure 4O; Rolls et al., 2008) or motifs of activity (Luczak et al., 2009) made up of recurrent pattern coactivation (ensembles) and co-suppression (decorrelated cell pairs). Interestingly, the distinctness of these patterns appeared to be altered after KET and in $Df(16)A^{+/-}$ (Figures 4B, 4D, 4F, and 4H). To quantify this at the group level, we performed a variant of the "gap test" (Clementz
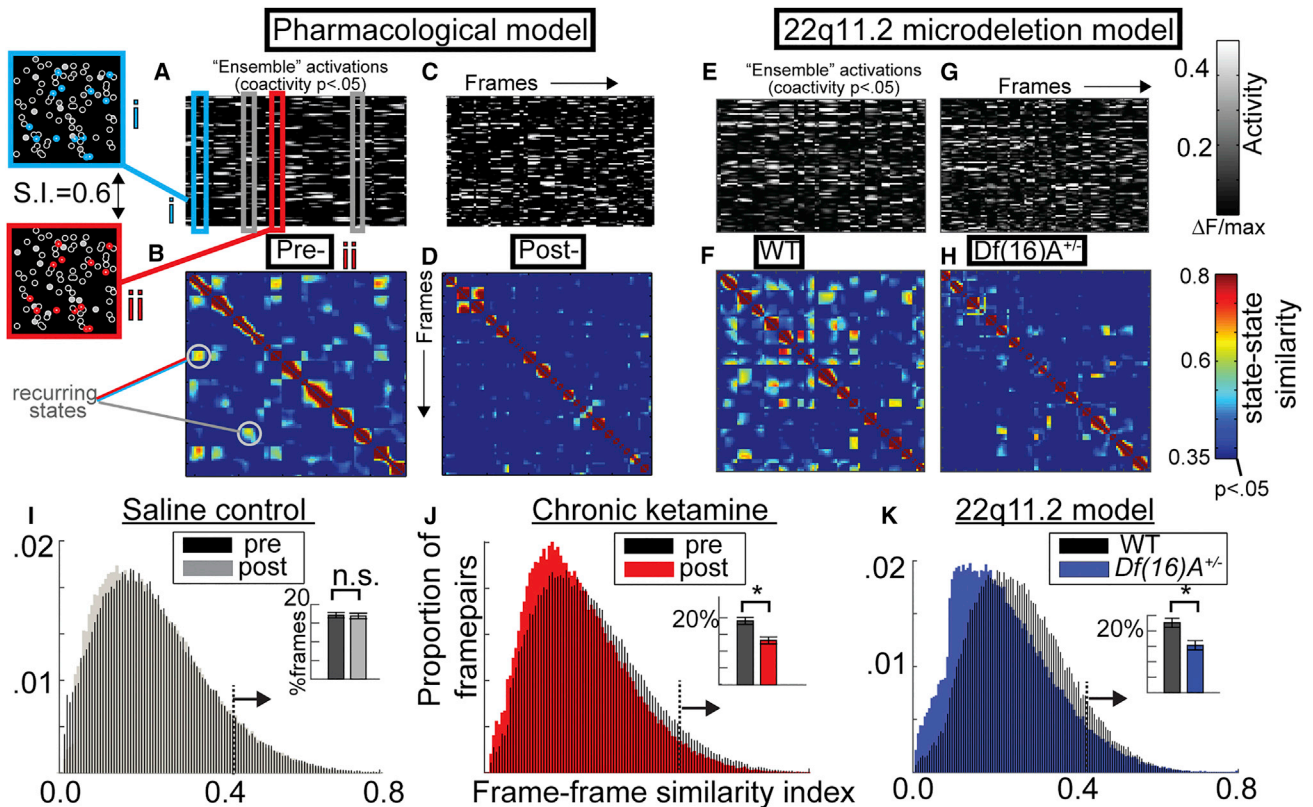
Figure 3. Unreliable Ensemble Activity in KET and *Df(16)A*[+/−] Mice

(A and B) Raster plot of single-neuron activity from one mouse during statistically defined ensemble activations (A) and a frame-by-frame matrix of similarity (B) (SI; symmetric along diagonal) demonstrating reoccurring population-wide activity patterns (>60% similarity) are depicted alongside the spatial distribution (left) of one repeating ensemble.

(C–H) Plots are repeated for (C and D) chronic KET and (E–H) in the *Df(16)A*[+/−] model.

(I–K) Histograms of SI from all state-state pairs along with inset barplots depicting proportion of statistically similar ensemble activations (p < 0.01) for (I) SAL, (J) KET, and (K) *Df(16)A*[+/−] (neuronal populations from n^{sal} = 6, n^{ket} = 6, n^{df16} = 7, $n^{control}$ = 7 mice; error bars reflect SEM across mice; I and J reflect within-subject SEM across mice [i.e., pre- versus post-]).

et al., 2016; Yan and Ye, 2007) using k-means analyses with k = 2–15. As the number of fitted cluster centroids ("k") increases, the within-cluster distances necessarily decrease. The degree to which an added centroid reduces distances approached zero and became linear between 4 and 7, suggesting that in local populations of ~75 neurons, one can expect 4–7 distinct patterns of activity to recur during 20 min of rest (similar to previous measurements; Carrillo-Reid et al., 2015). In general, KET and *Df(16)A*[+/−] mice showed higher within-cluster distances (Figures 4I–4K) and significantly smaller reductions of within-cluster distances with the inclusion of additional clusters in the models (Figures 3L–3N; F^{ket}(1,10) = 5.33, p < 0.05; $F^{df(16)A+/−}$(1,12) = 4.40, p < 0.05).

Our results are consistent with the hypothesis that both mouse models of SZ demonstrate an essential disorganization of ensemble activity rather than, for instance, an increased number of ensembles or network patterns. This degradation of neuronal ensembles was present in both models of SZ pathophysiology and/or genetic risk despite differences at the LFP, single-neuron, or pairwise connectivity levels (Figure 8A).

Abnormal Ensembles Reflect Chronic Alteration of Neocortical Circuits

Although psychotic episodes can appear transiently in psychiatrically healthy individuals, due to drug use or sleep deprivation, for example, SZ is a chronic disorder with persistent deficits in cognition and information processing that even precede the first psychotic episode for years (Kahn and Keefe, 2013). Because of this, we next explored whether the disorganization of functional neuronal ensembles identified in KET and *Df(16)A*[+/−] mice could reflect chronic pathological changes to brain function or whether more transient disruptions in neurotransmission could also generate these effects. First, we tested whether a single dose of subanesthetic KET could affect ensemble activity. In addition to eliciting transient SZ-like positive, negative, and cognitive symptomology in humans (Krystal et al., 1994), acute subanesthetic doses of KET induce hyperlocomotion, electrophysiological, and other behavioral abnormalities in rodents (Amann et al., 2010; Kocsis et al., 2013). To test this, we repeated 2P-Ca^{2+} imaging experiments described above, measuring local neuronal ensembles during awake rest in an additional set of
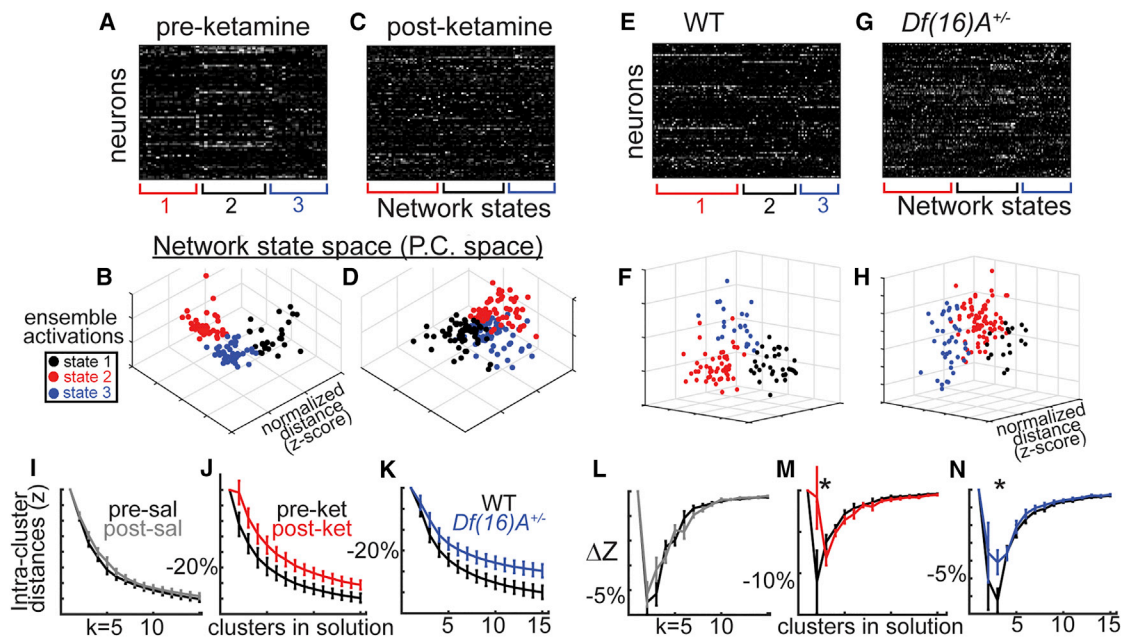
Figure 4. Disorganized Ensemble Activity in KET and *Df(16)A*$^{+/-}$ Mice

(A and B) k-means clustering (k = 3) on spontaneous ensemble activations (A), plotted in principal component space (B) (first three PCs) from example mice, demonstrates internally reliable and externally distinct repeating states, or putative "ensembles."

(C–H) Post-KET (C and D) and in *22q11.2* model (E–H).

(I–N) k-means was repeated across for k = 2–15 plotting (I–K) within-cluster distances and (L–N) decreases of within-cluster distances with added clusters (neuronal populations from n^{sal} = 6, n^{ket} = 6, n^{df16} = 7, $n^{control}$ = 7 mice; error bars reflect SEM across mice; I, J, L, and M reflect within subjects SEM across mice).

mice at baseline, after SAL injection, and after 15 mg/kg subcutaneous KET injection (n = 7 mice, 332 cells pre and post; 30 min after injection). As expected, a single treatment of subanesthetic KET (but not an equivalent volume of SAL) increased locomotion (Figure 5A; $F_{(2,6)}$ = 8.92, p < 0.01; $F^{base\ versus\ ket}_{(1,6)}$ = 6.96, p < 0.05). Although hyperlocomotion is not equivalent to any symptom of SZ or psychosis in humans (which can even involve amotivation, apathy, and reduced engagement in activities), it is a well-replicated effect in acute KET studies of mice, and our observation of this effect evinces the effectiveness of our paradigm. Acute KET also disinhibited ongoing activity when compared to baseline (during non-locomotive frames; Figure 5B; $F_{(2,662)}$ = 14.8, p < 0.001; $F^{base\ versus\ ket}_{(1,171)}$ = 11.56, p < 0.001), but pairwise correlations (Figure 5C; $F_{(2,6)}$ = 1.1, p = 0.35) and, importantly, the reliability of ongoing ensemble activations were clearly unaltered (Figure 5D; ($F_{(2,6)}$ = 2.10, p = 0.17; KET slightly but non-significantly *higher* than baseline).

In addition, it has been shown that both the KET and *Df(16)A*$^{+/-}$ models induce anatomical alterations in PV interneurons (Behrens et al., 2007; Fénelon et al., 2013), a well-established cortex-wide abnormality in human SZ patients (Hashimoto et al., 2008). GABAergic pathophysiology is not limited to PV interneurons in SZ (e.g., somatostatin-containing and cholesystokinin-containing interneurons also show changes; Fung et al., 2014), but given their dense local connectivity in neocortical circuits (Fino and Yuste, 2011) and their known role in modulating fast network synchrony (Sippy and Yuste, 2013; Sohal et al., 2009), it has been hypothesized that PV interneuron dysfunction

in particular may play a primary causal role in disrupting cortical computations underlying sensory processing and cognition (Javitt and Freedman, 2015; Lewis, 2014). In control experiments in the current study, using Pv:Cre::tdTomato mice, which express a red fluorescent indicator in PV interneurons enabling stable recording of calcium dynamics (Figure S7A), we confirmed in a subset of mice (n = 7; 56 cells) that activity levels in PV interneurons in V1 were stable a week after SAL but decreased after chronic KET (Figures S7B–S7E; see STAR Methods for detailed analyses and results). Because of this, we further sought to address whether transient decreases in local PV interneuron activity alone could affect ensemble activity and explain our population-level results.

Inhibitory DREADD channel hM4Di functionally silences host cells primarily through the suppression of synaptic current amplitude and release (Roth, 2016). Using awake pharmacogenetic suppression protocol methods (Hamm and Yuste, 2016; Jackson et al., 2016) we virally expressed hM4Di specifically in PV interneurons using the cre-lox system (Sohal et al., 2009) and recorded LFPs and 2P-Ca^{2+} dynamics before and after subcutaneous injection of clozapine N-oxide (12 mg/kg CNO; a typically inert ligand that activates hM4Di) in PV-hM4DI mice (n = 7 mice; 429 cells pre, 396 cells post) or controls (n = 5 mice; 356 cells pre, 349 cells post). DREADD suppression of local PV interneurons in the current study did not alter locomotion (Figure 5E), but as expected, PV interneuron suppression generally increased average Δf/f values in the local population (Figure 5F; $F^{PVhM4D}_{(1,824)}$ = 18.49, p < 0.001;
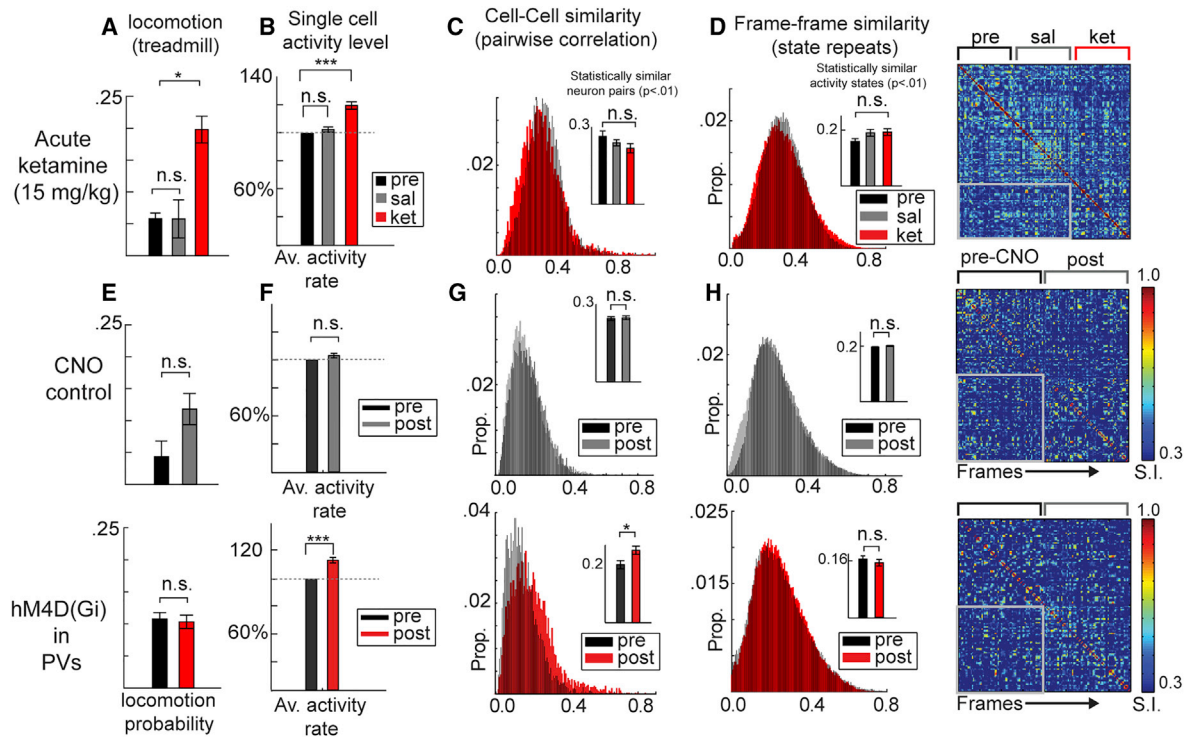
Figure 5. Acute KET and Interneuron Suppression Do Not Affect Ensemble Reliability

(A and B) Expected increases in (A) locomotion frequency (percent of frames recorded during locomotion) and (B) single-neuron activity were observed after 15 mg/kg acute KET compared to SAL control (332 cells base, post-SAL, post-KET).

(C and D) Functional correlations among all neuron pairs (C) and consistency of ensemble activations (D) were unaltered after acute KET, as population states repeated within and across (gray box) treatment periods (each 20 min).

(E–H) CNO control experiments (mice injected only with GCaMP6; above; 356 cells pre, 349 cells post) are compared to DREADD suppression (hM4D(Gi); 429 cells pre, 396 cells post) of parvalbumin-containing (PV) interneuron experiments. (E) Locomotion was not affected but (F) single-neuron activity and (G) the proportion of significantly coactive neuron pairs increased. (H) Ensemble activations nevertheless maintained reliable patterns of activity across time (*p < 0.05;***p < 0.001; one-way ANOVA; loco/neuronal populations from $n^{ket} = 7$, $n^{pv-hM4D} = 7$, $n^{cno-control} = 5$ mice; error bars reflect within-subject SEM across mice; B and F reflect within-cell SEM across cells).

$F^{control}(1,706) = 0.88$, p = 0.34). The proportion of correlated cell pairs showed a clear increase after PV interneuron suppression ($F^{PVhM4D}(1,6) = 6.64$, p < 0.05; $F^{control}(1,4) = 0.09$, p = 0.77; Figure 5G) and a more straightforward change in population coactivity than in the chronic models. It is important to point out that while PV interneurons may facilitate short timescale spike synchrony, organizing spike timing in coactivated neurons by supporting gamma-band oscillations (Sohal et al., 2009), our effect indicates that shared variations in firing rates between neurons over longer time courses (seconds to minutes) are suppressed or modulated by PV interneurons, an effect that converges with previous experiments in thalamocortical slices (Sippy and Yuste, 2013). Further, this increase in pairwise correlations was nevertheless not accompanied by any change in ensemble reliability, as the number of significant framepairs (state repeats) was again unchanged ($F^{PVhM4D}(1,6) = 0.27$, p = 0.62; $F^{control}(1,4) = 0.09$, p = 0.77; Figure 5H).

Thus, NMDAR blockade or local PV interneuron suppression was sufficient to disinhibit neurons at similar levels as chronic KET, increase locomotion, and/or alter correlations between local neuronal pairs, but neither manipulation disrupted the reli-

ability of local ensemble activity. Altogether this suggests that chronic models of SZ and potentially the disease itself involve a breakdown of stable neocortical activity patterns, and this disruption is beyond the effects that short-term disruptions in local excitatory/inhibitory balance have on local circuit function. Further, our results challenge the notion that any disruption of excitatory or inhibitory neurotransmission can disrupt existing ensemble patterns in the cortex, and emphasize that ensemble disorganization is not a simple computational or mechanistic consequence of alterations in single-neuron activity or average correlation values. Like our results, past studies have shown acute blockade of NMDARs is sufficient to disinhibit brain activity and cause other transient sensory and cognitive disturbances (Kargieman et al., 2007; Yang et al., 2014), perhaps through a suppression of GABAergic cells in the thalamic reticular nucleus (Kargieman et al., 2007). Yet chronic mouse models of KET and genetic mouse models of SZ involve longer-lasting changes to dendritic spine stability and local inhibitory interneuron populations (Behrens et al., 2007; Featherstone et al., 2012; Fénelon et al., 2013), and these changes may together give rise to a lasting disorganization of local neuronal ensembles.
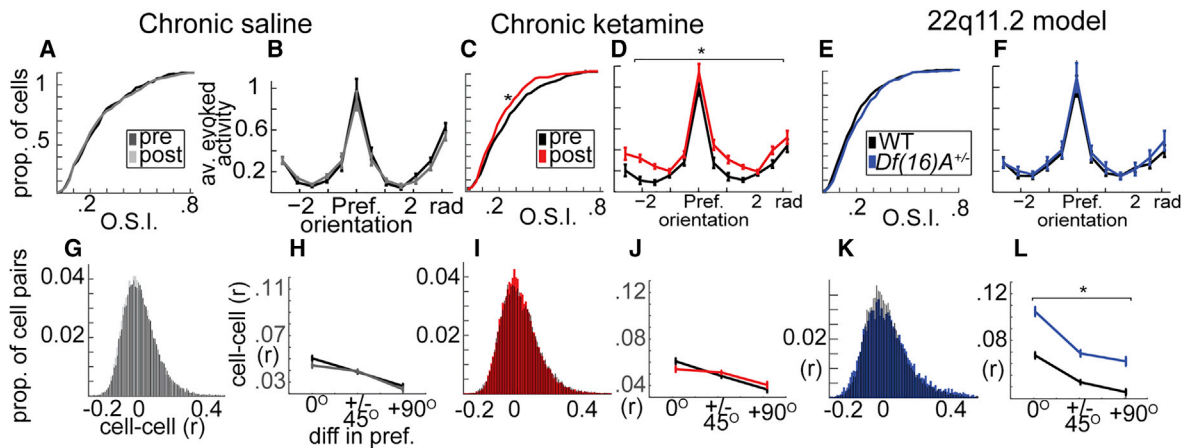
Figure 6. Sensory Stimulus-Evoked Responses and Pairwise Variability Are Altered in KET and *Df(16)A*$^{+/-}$ Mice

(A–F) Orientation selectivity (OSI) (A) and trial-averaged response curves (B) from visually responsive neurons from SAL-treated mice (pre versus post, n = 631 total cells), chronic KET-treated mice (pre versus post, n = 596) (C and D), and *Df(16)A*$^{+/-}$ mice (E and F) compared to littermate controls (n = 582).

(G–J) Shared variability among neuron pairs across presentations of the same stimulus (G) ("noise correlations"; same cells from A) varied with respect to the orientation preference similarity of neuron pairs (H) and was not affected by KET (I and J).

(K and L) *Df(16)A*$^{+/-}$ mice, on the other hand, showed an increase in noise correlations among all neuron pairs in the local population regardless of whether they shared stimulus preferences.

Line plots reflect average cell responses relative to their preferred stimulus (pre-treatment, B and D; within mouse, F), and/or including only cells with >0.1 OSI (H, J, and L) (*p < 0.05; one-way ANOVA; n^{sal} = 6, n^{ket} = 6, n^{df16} = 7, $n^{control}$ = 7 mice; error bars reflect SEM across cells/cell pairs).

Ensemble-Level Dysfunction during Visual Stimulation in KET and *Df(16)A*$^{+/-}$

Finally, we inquired whether the functional disorganization of neuronal ensembles we observed in KET and *Df(16)A*$^{+/-}$ was specific to ongoing or awake "rest" activity, suggesting a principle abnormality of intrinsic activity (Whitfield-Gabrieli and Ford, 2012), or perhaps also extended to stimulus-elicited brain states, suggesting a more general circuit pathology. If so, this would suggest a deficit in externally driven information processing, possibly accounting for persistent perceptual deficiencies in SZ (Javitt and Freedman, 2015).

As above, we first examined single-neuron activity, pairwise correlations, and ensemble-wise functional characteristics in V1 circuits in both models, but not during visual stimulation. We presented awake mice with 3 s, square wave moving gratings (100% contrast, 0.04 cycles per degree, 2 cycles per second, 7–8 s gray screen interstimulus interval) of six different orientations (0, 30, 60, 90, 120, and 150 degrees; 10–14 repeats each). V1 neurons respond selectively to contours of particular orientations in their visual field and this selectivity can be quantified by the orientation selectivity index, OSI (Niell and Stryker, 2008) (Figures S2F and S2H). In our study, neurons showing significant stimulus-driven activity (average stimulus-induced ΔF greater than 1.67 SD above baseline fluctuation; Hamm and Yuste, 2016; 70%–75% of neurons) maintained the same preferred stimulus orientation prior to minipump insertion and 1 week after for the SAL or KET treatment (Figure S8), but KET mice showed significantly decreased quantitative OSI values (n^{KET} = 6 mice, 297/299 cells pre/post; n^{SAL} = 6 mice, 320/311 cells; $F^{interaction}$(1,1223) = 8.4, p < 0.01; F^{sal}(1,629) = 1.25, p = 0.26; F^{ket}(1,594) = 9.73, p < 0.01; Figures 6A–6C and S8). Examining stimulus response curves demonstrated significant

increases in activity driven across all stimuli (F^{week}(1,594) = 6.01, p < 0.05; $F^{weekBYorientation}$(11,594) = 0.77, p = 0.67; Figure 6D), suggestive of a decrease in subtractive inhibition or gain modulation (Lee et al., 2014), another effect consistent with PV interneuron dysfunction seen in KET mice in the current study (Figure S7). Interestingly, neurons from *Df(16)A*$^{+/-}$ mice did not differ from neurons from littermate controls on OSIs ($n^{Df(16)A+/-}$ = 7 mice, 336 cells; n^{WT} = 7 mice, 246 cells; F(1,580) = 0.96, p = 0.32; Figure 6E) and exhibited equivalent stimulus response curves that did not differ (Figure 6F; F^{grp}(1,580) = 0.94, p = 0.33; $F^{grpBYorientation}$(11,580) = 0.66, p = 0.77). Thus, similar to what was observed during ongoing activity during awake rest, the KET model involved disinhibition at the single-neuron level while *Df(16)A*$^{+/-}$ mice showed no such abnormality.

During sensory stimulation, neocortical circuits display dynamic changes in correlated activity among neuronal pairs (Averbeck et al., 2006). While correlations arise necessarily due to shared responses to an external stimulus (or "signal correlation"), an additional source of correlations is shared variability across otherwise similar events (Hofer et al., 2011). In other words, individual neurons do not respond identically to the same stimulus over and over, and when this variability is shared among neurons in a local network, it is referred to as "noise correlation." While the computational consequences of noise correlation are debated and complex (Averbeck et al., 2006), an excess amount of noise correlation could be detrimental to reliable stimulus encoding (Cohen and Maunsell, 2009). Here we focused on noise correlation across stimulus presentations (within the same orientation, then averaged across orientations) within neuron pairs using similar methods as previously reported (Hofer et al., 2011). While neither SAL nor KET affected noise correlations (F^{sal}(1,26488) = 3.26,

p = 0.08; $F^{ket}(1,21004) = 0.23$, p = 0.97; Figures 6G–6J; $pairs^{KETpre} = 12,600$, $pairs^{KETpost} = 9,238$, $pairs^{SALpre} = 13,894$, $pairs^{SALpost} = 11,772$; $n^{KET} = 6$ mice; $n^{SAL} = 6$ mice), $Df(16)A^{+/-}$ showed abnormally increased average noise correlations among all neuron pairs ($F^{group}(1,15656) = 152.48$, p < 0.001; Figure 6K; $pairs^{df16} = 9,442$, $pairs^{WT} = 6,282$; $n^{Df(16)A+/-} = 7$ mice; $n^{WT} = 7$ mice). As expected, noise correlations were modulated by the similarity of the preferred orientation of neurons, with neuron pairs sharing the same preferred orientation showing higher noise correlation than pairs with opposite preferred orientations (focusing only on OSIs > 0.1; Mazurek et al., 2014; pairs = 15,724; 14 mice; $F(2,15656) = 88.79$, p < 0.001). Although a significant group by orientation interaction effect was present ($F(2,15656) = 3.23$, p = 0.03), it was small relative to the group effect, which was substantial regardless of whether neuron pairs shared orientation preference (Figure 6L). Again, similar to effects seen during ongoing activity, no change was seen in the proportion of significantly noise-correlated neuron pairs present ($F(1,11) = 1.39$, p = 0.24).

While both KET and $Df(16)A^{+/-}$ showed some abnormalities in stimulus-evoked activity in V1 at single- and pairwise neuronal levels, the nature of these effects diverged, with KET showing single-neuron disinhibition and $Df(16)A^{+/-}$ showing augmented noise correlations. We next examined whether a clear deficit in ensemble regularity could again serve as a downstream convergence point for these distinct abnormalities in low-level visual stimulus processing, similar to what we observed during ongoing ensemble activity during awake rest. First we demonstrated that stimulus-evoked ensembles showed relative consistency (significant similarity) during and across repeated presentations of the same stimulus (i.e., grating orientation; Figures 7A and 7B, left panel). This characteristic was attenuated after KET (Figures 7C and 7D) and in $Df(16)A^{+/-}$ mice relative to littermate controls (Figures 7E–7H) in representative samples. Figures 7I–7L further illustrate this effect using a PCA-derived projection of the multi-neuronal state space onto three dimensions, showing that the trajectory of the local population activity state during visual stimulation is consistent within and distinct between orientation angles (separate PCA for each condition using average trial data and neurons as variables; each trial is a line; each orientation angle is a different shade of gray). These properties were diminished in the disease models (Figures 7J and 7L). To quantify this, we calculated the relative change in between-trial population similarity (SI; see above) from baseline (pre-stimulus, 1 s), averaging over the stimulus presentation period (3 s), and normalizing it by the SD of similarity values derived from a bootstrapped distribution of "random" similarity values derived by shuffling each mouse's population activity (Figure S5E). This generated a Z score metric for each trial for each mouse.

As expected, cross-trial similarity varied as a function of orientation difference between trials (i.e., trials with the same orientation evoke more similar population states than different orientations; $F^{orientation}(2,12) = 22.57$, p < 0.001), yet some similarity above chance 0 was shared even among non-similar orientations. These stimulus-evoked population states were stable before and after SAL treatment (Figures 7D–7G; $F^{group}(1,36) = 0.09$, p = 0.77; $n^{SAL} = 6$ mice) but became less reliable after KET treatment (Figures 7D–7G; $F^{group}(1,36) = 7.58$, p < 0.05;

$n^{KET} = 6$ mice) and in the $Df(16)A^{+/-}$ mice ($F^{group}(1,41) = 5.78$, p < 0.05; $n^{Df(16)A+/-} = 7$ mice; $n^{WT} = 7$ mice). A group by orientation interaction effect did not reach significance for either model (p > 0.05). Thus, activity states in local populations of neurons that encode visual stimuli are unreliably activated by external stimuli in our mouse models, supporting the notion that a generalized disorganization of functional neocortical ensembles could undermine short-term memory processes and/or the stable encoding of the environment (Hopfield, 1982; Rolls et al., 2008), providing a basis to explain the symptomology of SZ.

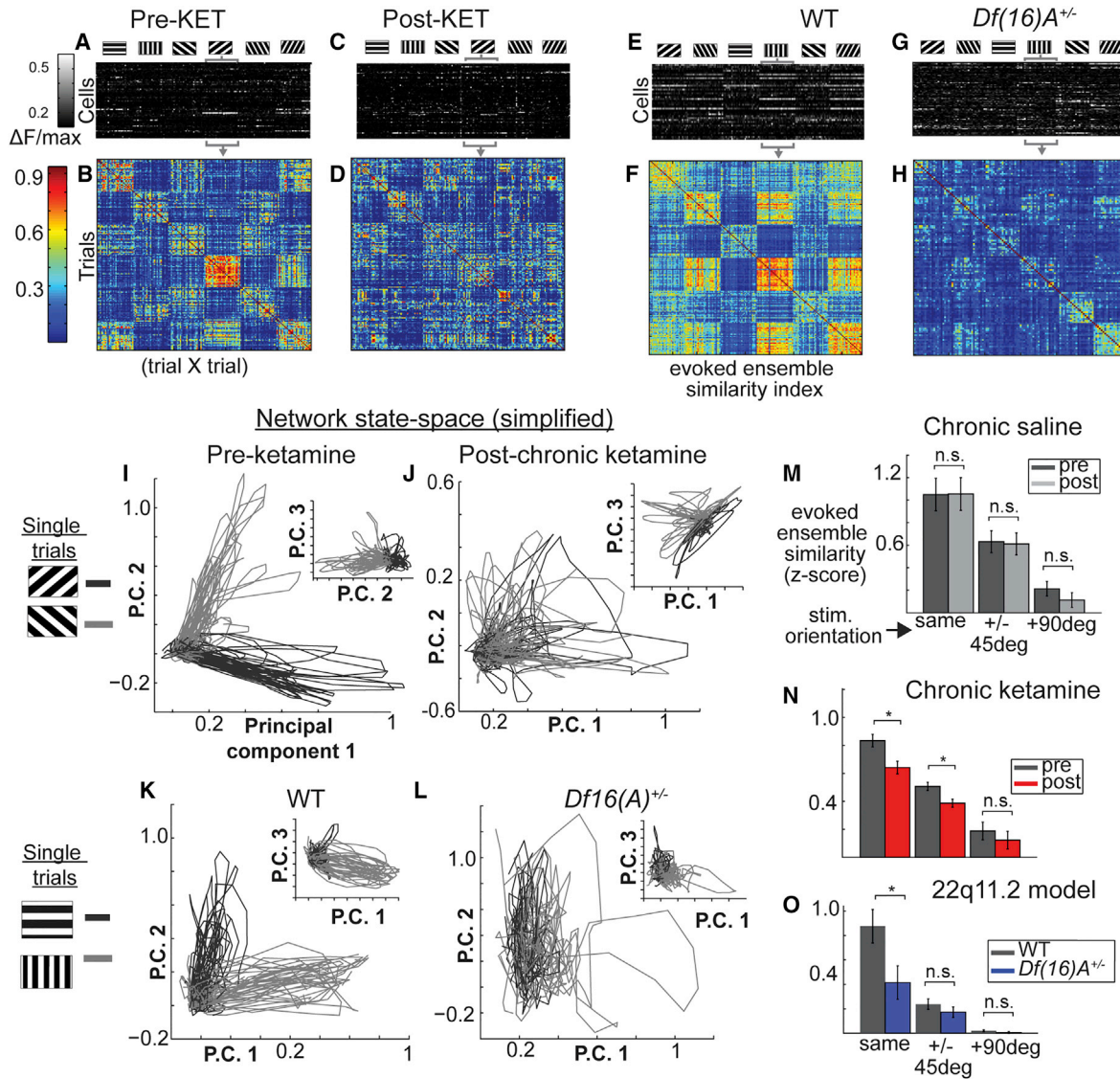## DISCUSSION

Altered Neuronal Ensembles in Two Mouse Models of SZ

We examined here the functional dynamics of local cortical circuits in two distinct models of SZ-relevant brain pathophysiology: a pharmacological model (KET) and a genetic model, which additionally offered construct validity by recapitulating in mice a strong causal factor for the disease (i.e., 22q11.2 microdeletions).

At the level of LFPs, which offer a gross-level estimate of cortical activity levels and broad-scale synchrony, these models generally recreated one of the most established endophenotypes of SZ (decreased stimulus-elicited gamma-band transients), but differed in the degree to which background activity levels were augmented (Figure 8). Further, at the single-neuron level, KET disinhibited neurons, leading to larger calcium transients and reduced orientation selectivity, while $Df(16)A^{+/-}$ did not differ from their littermate controls. Next, at the average pairwise level (correlations), both models showed what appeared to be a dysregulation of synchrony, but the nature of this change was not straightforward, showing no change in strongly correlated neuron pairs despite a change in mean "similarity values." Correlations among cell pairs across repeated visual stimulations, or "noise correlations," also differentiated KET and genetic models, wherein only $Df(16)^{+/-}$ showed augmentations.

Yet where these models converged was at the ensemble level, when local multineuronal activity patterns were measured across time. Both models showed a systematic decrease in state reliability across ensemble activations at rest and during direct visual stimulation. Importantly, this decrease was not a simple consequence of shared single-neuron activity level changes or strengthening/weakening of functional correlations, since neither disinhibition nor orientation selectivity nor pairwise correlations alone could predict the ensemble-level abnormalities apparent only in our chronic models. Instead, our results likely reflect a disorganization of emergent multineuronal dynamics.

Chronic Manipulations Are Necessary for Altered Ensembles

Acute KET blockade of NMDARs and pharmacogenetic suppression of PV interneuron protocols employed in the current study were sufficient to disinhibit neuronal activity at similar levels as chronic KET, yet neither manipulation was sufficient to disorganize ensemble-level activity like in our chronic models. This finding is mechanistically informative in two ways. First, local population activity patterns are stable in a healthy brain

Figure 7. Stimulus-Evoked Network States Are Altered Similarly in KET and *Df(16)A*$^{+/-}$ Mice

(A) Pre-treatment single-trial activity (Δf) from individual cells (rows), averaged within trials (columns) and sorted by stimulus orientation.

(B) Cross-trial similarity matrix from trials in (A) (similarity index, SI).

(C–H) Same plots (C and D) after KET, (E and F) in littermate controls, and (G and H) in *Df(16)A*$^{+/-}$.

(I–L) Population activity projected with PCA into three-dimensional space (each line is one trial; shade of gray denotes stimulus orientation). Similar ensemble activations show similar line trajectories from origin.

(M–O) Average trial-evoked ensemble similarity (*p < 0.05, one-way ANOVA; neuronal populations from n^{sal} = 6, n^{ket} = 6, n^{df16} = 7, $n^{control}$ = 7 mice; error bars reflect within-subject SEM across mice; O reflects SEM across mice).

state (Figure S6D), but we have recently shown that with persistent and direct perturbation at the microcircuit level, ensembles in adult brains can be programed or "imprinted" (Carrillo-Reid et al., 2016). Thus, while acute KET may disinhibit neuronal activity, chronic NMDAR blockade or a genetic lesion (22q11.2 microdeletions) additionally results in a persistent destabilization of synapses and dendritic spines (Fénelon et al., 2013), essentially deprogramming local ensembles that are the cortical building blocks necessary for stable cognition. Indeed, many aspects of SZ brain pathology involve deviant developmental trajectories

or exacerbation over time (Walterfang et al., 2008), so future work could characterize ensemble organization across various periods of development in relevant mouse models.

Second, it has been previously shown that chronic, but not acute, NMDAR blockade is sufficient to alter local inhibitory interneuron populations (PV interneurons; Behrens et al., 2007), an effect that we replicate in the functional domain (Figure S7). PV interneurons play a critical role in organizing stimulus-elicited local gamma synchrony and pairwise correlations (Figure 5G; Sippy and Yuste, 2013; Sohal et al., 2009), yet our
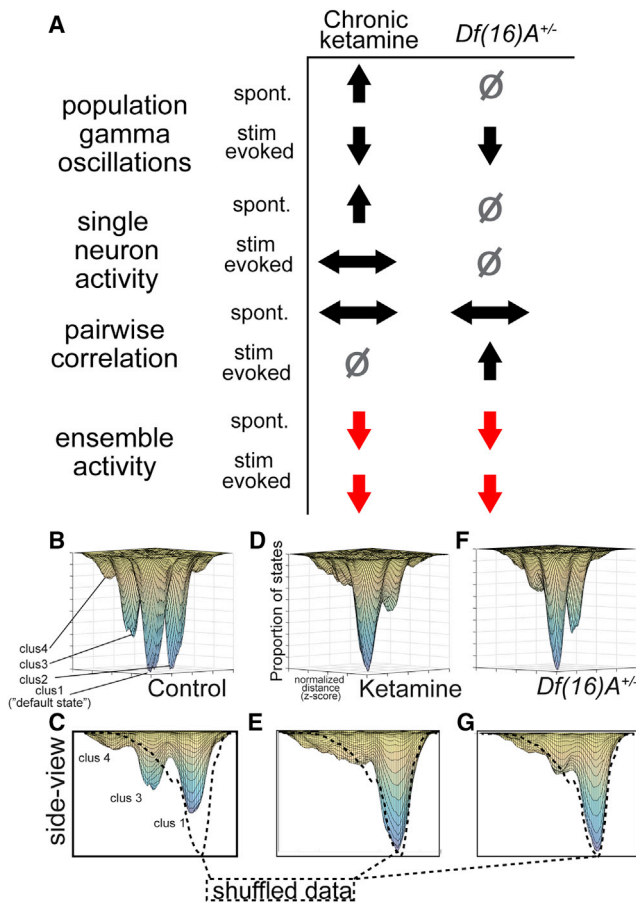
Figure 8. Summary of Effects and Model for Attractor Pathophysiology of SZ

(A) LFP, cell-wise, pairwise, and ensemble-wise effects in both models demonstrate that ensemble-level deficits are the most consistent across models and conditions. Comparing to control animals, up arrows signify an increase; down arrows a decrease; left/right a change in distribution; square is no change.

(B) Iterative combination of k-means solutions across mice, where spontaneous ensemble activations were assigned to "clusters" based on cluster sizes, and clusters were assigned to a specific location on a two-dimensional PCA-derived map, organized spatially based on average inter-cluster distances within a group.

(C) Results after shuffling ensemble activations (across cells, 1,000×) indicate that fully disorganized network activity would result in a single "default state" represented by a single Gaussian peak (dotted line on right).

(D–G) Control mice (pre-treatment/homozygous littermates), but not disease model mice, showed a number of clear peaks, suggestive of attractors in the network (neuronal populations from $n^{WT} = 7$, $n^{ket} = 6$, $n^{df16} = 7$ mice).

results suggest that suppressing PV interneurons alone is again insufficient to produce the ensemble-level deficits seen in both mouse models. This demonstration alone does not exclude a causal role of PV interneuron in SZ. PV interneuron dysfunction in the disease could play a developmental role, or, intriguingly, the effect PV interneurons have on the network may even scale nonlinearly with the degree of their suppression (e.g., partial suppression disinhibits other interneurons more than pyramidal neurons). Further, GABAergic pathophysiology in SZ is not limited to

a simple decrease in PV interneuron activity, but involves complex changes that may vary at the subcellular level depending on the PV interneuron cell subtype (Lewis et al., 2012) and also involves other subtypes including somatostatin and cholesystokinin interneurons (Fung et al., 2014). Still, we provide some evidence that changes and, in particular, long-term changes in excitatory neurotransmission are critical for cortical assembly disorganization, perhaps insofar as synaptic stability and plasticity are affected. So while our chronic KET and $Df(16)A^{+/-}$ models both alter inhibitory neurotransmission to various degrees, our results, together with recently accumulating evidence from large-scale genetic studies of SZ (Hall et al., 2015), suggest a critical (if not primary) role of glutamatergic synaptic deficits in the disease etiology (Poels et al., 2014).

SZ as an Attractor Disease

These results are consistent with an "attractor" theory of SZ (Rolls et al., 2008), in which the critical pathophysiology of the disease involves altered multineuronal dynamics. The repeating activity patterns described in this report could be naturally interpreted as representing cortical "attractors" (Hopfield, 1982) or the preferred, semi-stable activity patterns in the neocortical network involving recurrently coactive groups of neurons (or ensembles; Miller et al., 2014) (Rolls et al., 2008). Our observed lack of reliability in the population-wide activity states observed in both mouse models of SZ pathophysiology, both at rest and during direct visual stimulation, is consistent with an alteration in cortical attractors, resulting in an effective "shallowing" of the cortical attractor landscape, wherein percepts, short-term memories, or computational outcomes become highly unstable (Rolls et al., 2008). To illustrate this possibility quantitatively, we utilized the solutions of the k-means clustering analysis described above, fixing the number of clusters to k = 6 (based on Figures 4L–4N) and repeating the analysis 50 times for all multineuronal datasets measured. We iteratively assigned ensemble activations to clusters, and cluster centroids to a specific place in a two-dimensional plane, arranged by relative size of the cluster groups (largest cluster at the plane origin) and separated by average cluster-to-cluster centroid distances across all mice within a condition (Figures 8B–8G). While a bootstrapped fully random distribution of "events" (based on shuffled recorded data from each mouse) resulted in a single Gaussian "valley" centered on the spot of the first "cluster" (the origin), recorded data from healthy circuits showed the emergence of multiple "valleys" (Figures 8B and 8C), or putative attractors (highly probable patterns in the space of possible activity states). KET and $Df(16)A^{+/-}$ data can therefore be interpreted, with this demonstration, as showing a shallowing of the attractor landscape in favor of one continuous distribution of possible activity states (Figures 8D–8G). Elucidating the exact meaning of observed, repeating population states described herein is a key focus of ongoing work requiring further study and perhaps a substantial advancement in measuring or stimulating neurotechnology, including the ability to record and manipulate all or most of the neurons in an intact, behaving organism (Alivisatos et al., 2012).

In closing, we have established that unreliable and indistinct ensemble activity in sensory cortex is present in two separate

mouse models of SZ-relevant pathophysiology and/or risk. Our data suggest that changes affecting ensemble reliability across time may represent a key emergent convergence point for lower-level abnormalities. Causally linking local ensemble dysfunction to alterations in global networks like those seen in SZ patient samples (Yang et al., 2014) or to perceptual or cognitive dysfunction fundamental to SZ (Javitt and Freedman, 2015) is a feasible next step given the recently established ability to carry out complex head-fixed behavioral studies in mice (Harvey et al., 2012). Future work with even more diverse disease models will be informative, keeping in mind that the utility of a model rests not necessarily in whether or how well it recapitulates the disease but in how it is employed to test specific hypotheses (Gordon and Moore, 2012). But intriguingly, the ability to selectively activate, reinforce, and imprint neocortical ensembles (Carrillo-Reid et al., 2016) could offer a novel therapeutic approach to SZ via the reprogramming of cortical circuits to restabilize an altered attractor landscape and potentially reverse some of the symptoms of the disease. Finally, our results not only support and refine new computational hypotheses regarding how neuronal circuit dysfunction relates to the phenomenology of the disease, but they also underscore the hypothesis that reliable ensemble activations and attractor states comprise likely building blocks of perception and thought.

STAR★METHODS

Detailed methods are provided in the online version of this paper and include the following:

- KEY RESOURCES TABLE
- CONTACT FOR REAGENT AND RESOURCE SHARING
- EXPERIMENTAL MODEL AND SUBJECT DETAILS
- METHOD DETAILS
  - Animals, Surgery, and Training
  - Genotyping of $Df(16)A^{+/-}$ mice
  - Two-Photon Calcium Imaging
  - Visual Stimulation
  - Local Field Potential recordings
  - Acute ketamine and pharmacogenetic suppression of PVs
  - Study of Parvalbumin-containing Interneurons
- QUANTIFICATION AND STATISTICAL ANALYSIS
  - Spectral analysis of LFP
  - Image Analysis
  - Single cell analyses
  - Pairwise analysis
  - Population analysis
  - Analysis of stimulus evoked activity
  - Acute ketamine and PV-suppression experiments
  - Analysis of PV interneurons
- ADDITIONAL RESOURCES

SUPPLEMENTAL INFORMATION

Supplemental Information includes eight figures and can be found with this article online at http://dx.doi.org/10.1016/j.neuron.2017.03.019.

REFERENCES

Alivisatos, A.P., Chun, M., Church, G.M., Greenspan, R.J., Roukes, M.L., and Yuste, R. (2012). The brain activity map project and the challenge of functional connectomics. Neuron 74, 970–974.

Amann, L.C., Gandal, M.J., Halene, T.B., Ehrlichman, R.S., White, S.L., McCarren, H.S., and Siegel, S.J. (2010). Mouse behavioral endophenotypes for schizophrenia. Brain Res. Bull. 83, 147–161.

Arguello, P.A., and Gogos, J.A. (2012). Genetic and cognitive windows into circuit mechanisms of psychiatric disease. Trends Neurosci. 35, 3–13.

Averbeck, B.B., Latham, P.E., and Pouget, A. (2006). Neural correlations, population coding and computation. Nat. Rev. Neurosci. 7, 358–366.

Behrens, M.M., Ali, S.S., Dao, D.N., Lucero, J., Shekhtman, G., Quick, K.L., and Dugan, L.L. (2007). Ketamine-induced loss of phenotype of fast-spiking interneurons is mediated by NADPH-oxidase. Science 318, 1645–1647.

Brenner, C.A., Krishnan, G.P., Vohs, J.L., Ahn, W.Y., Hetrick, W.P., Morzorati, S.L., and O'Donnell, B.F. (2009). Steady state responses: electrophysiological assessment of sensory function in schizophrenia. Schizophr. Bull. 35, 1065–1077.

Buzsaki, G. (2009). Rhythms of the Brain (Oxford University Press).

Carlén, M., Meletis, K., Siegle, J.H., Cardin, J.A., Futai, K., Vierling-Claassen, D., Rühlmann, C., Jones, S.R., Deisseroth, K., Sheng, M., et al. (2012). A critical role for NMDA receptors in parvalbumin interneurons for gamma rhythm induction and behavior. Mol. Psychiatry 17, 537–548.

Carrillo-Reid, L., Miller, J.E., Hamm, J.P., Jackson, J., and Yuste, R. (2015). Endogenous sequential cortical activity evoked by visual stimuli. J. Neurosci. 35, 8813–8828.

Carrillo-Reid, L., Yang, W., Bando, Y., Peterka, D.S., and Yuste, R. (2016). Imprinting and recalling cortical ensembles. Science 353, 691–694.

Chatterjee, M., Verma, R., Ganguly, S., and Palit, G. (2012). Neurochemical and molecular characterization of ketamine-induced experimental psychosis model in mice. Neuropharmacology 63, 1161–1171.

Chen, T.-W., Wardill, T.J., Sun, Y., Pulver, S.R., Renninger, S.L., Baohan, A., Schreiter, E.R., Kerr, R.A., Orger, M.B., Jayaraman, V., et al. (2013). Ultrasensitive fluorescent proteins for imaging neuronal activity. Nature 499, 295–300.

Clementz, B.A., Sponheim, S.R., Iacono, W.G., and Beiser, M. (1994). Resting EEG in first-episode schizophrenia patients, bipolar psychosis patients, and their first-degree relatives. Psychophysiology 31, 486–494.

Clementz, B.A., Sweeney, J.A., Hamm, J.P., Ivleva, E.I., Ethridge, L.E., Pearlson, G.D., Keshavan, M.S., and Tamminga, C.A. (2016). Identification

of distinct psychosis biotypes using brain-based biomarkers. Am. J. Psychiatry 173, 373–384.

Cohen, M.R., and Maunsell, J.H.R. (2009). Attention improves performance primarily by reducing interneuronal correlations. Nat. Neurosci. 12, 1594–1600.

Cossart, R., Aronov, D., and Yuste, R. (2003). Attractor dynamics of network UP states in the neocortex. Nature 423, 283–288.

Delorme, A., and Makeig, S. (2004). EEGLAB: an open source toolbox for analysis of single-trial EEG dynamics including independent component analysis. J. Neurosci. Methods 134, 9–21.

Driesen, N.R., McCarthy, G., Bhagwagar, Z., Bloch, M.H., Calhoun, V.D., D'Souza, D.C., Gueorguieva, R., He, G., Leung, H.-C., Ramani, R., et al. (2013). The impact of NMDA receptor blockade on human working memory-related prefrontal function and connectivity. Neuropsychopharmacology 38, 2613–2622.

Dubbs, A., Guevara, J., and Yuste, R. (2016). moco: fast motion correction for calcium imaging. Front. Neuroinform. 10, 6.

Featherstone, R.E., Liang, Y., Saunders, J.A., Tatard-Leitman, V.M., Ehrlichman, R.S., and Siegel, S.J. (2012). Subchronic ketamine treatment leads to permanent changes in EEG, cognition and the astrocytic glutamate transporter EAAT2 in mice. Neurobiol. Dis. 47, 338–346.

Featherstone, R.E., Shin, R., Kogan, J.H., Liang, Y., Matsumoto, M., and Siegel, S.J. (2015). Mice with subtle reduction of NMDA NR1 receptor subunit expression have a selective decrease in mismatch negativity: Implications for schizophrenia prodromal population. Neurobiol. Dis. 73, 289–295.

Fénelon, K., Xu, B., Lai, C.S., Mukai, J., Markx, S., Stark, K.L., Hsu, P.-K., Gan, W.-B., Fischbach, G.D., MacDermott, A.B., et al. (2013). The pattern of cortical dysfunction in a mouse model of a schizophrenia-related microdeletion. J. Neurosci. 33, 14825–14839.

Fino, E., and Yuste, R. (2011). Dense inhibitory connectivity in neocortex. Neuron 69, 1188–1203.

Fung, S.J., Fillman, S.G., Webster, M.J., and Shannon Weickert, C. (2014). Schizophrenia and bipolar disorder show both common and distinct changes in cortical interneuron markers. Schizophr. Res. 155, 26–30.

Glantz, L.A., and Lewis, D.A. (2000). Decreased dendritic spine density on prefrontal cortical pyramidal neurons in schizophrenia. Arch. Gen. Psychiatry 57, 65–73.

Gordon, J.A., and Moore, H. (2012). Charting a course toward an understanding of schizophrenia. Neuron 76, 465–467.

Hall, J., Trent, S., Thomas, K.L., O'Donovan, M.C., and Owen, M.J. (2015). Genetic risk for schizophrenia: convergence on synaptic pathways involved in plasticity. Biol. Psychiatry 77, 52–58.

Hamm, J.P., and Yuste, R. (2016). Somatostatin interneurons control a key component of mismatch negativity in mouse visual cortex. Cell Rep. 16, 597–604.

Hamm, J.P., Dyckman, K.A., McDowell, J.E., and Clementz, B.A. (2012). Precue fronto-occipital alpha phase and distributed cortical oscillations predict failures of cognitive control. J. Neurosci. 32, 7034–7041.

Hamm, J.P., Ethridge, L.E., Boutros, N.N., Keshavan, M.S., Sweeney, J.A., Pearlson, G.D., Tamminga, C.A., and Clementz, B.A. (2014). Diagnostic specificity and familiality of early versus late evoked potentials to auditory paired stimuli across the schizophrenia-bipolar psychosis spectrum. Psychophysiology 51, 348–357.

Harris, K.D., and Thiele, A. (2011). Cortical state and attention. Nat. Rev. Neurosci. 12, 509–523.

Harvey, C.D., Coen, P., and Tank, D.W. (2012). Choice-specific sequences in parietal cortex during a virtual-navigation decision task. Nature 484, 62–68.

Hashimoto, T., Bazmi, H.H., Mirnics, K., Wu, Q., Sampson, A.R., and Lewis, D.A. (2008). Conserved regional patterns of GABA-related transcript expression in the neocortex of subjects with schizophrenia. Am. J. Psychiatry 165, 479–489.

Hebb, D.O. (1949). The Organization of Behavior (Wiley).

Hirano, Y., Oribe, N., Kanba, S., Onitsuka, T., Nestor, P.G., and Spencer, K.M. (2015). Spontaneous gamma activity in schizophrenia. JAMA Psychiatry 72, 813–821.

Hiroi, N., Takahashi, T., Hishimoto, A., Izumi, T., Boku, S., and Hiramoto, T. (2013). Copy number variation at 22q11.2: from rare variants to common mechanisms of developmental neuropsychiatric disorders. Mol. Psychiatry 18, 1153–1165.

Hofer, S.B., Ko, H., Pichler, B., Vogelstein, J., Ros, H., Zeng, H., Lein, E., Lesica, N.A., and Mrsic-Flogel, T.D. (2011). Differential connectivity and response dynamics of excitatory and inhibitory neurons in visual cortex. Nat. Neurosci. 14, 1045–1052.

Hopfield, J.J. (1982). Neural networks and physical systems with emergent collective computational abilities. Proc. Natl. Acad. Sci. USA 79, 2554–2558.

Jackson, J., Ayzenshtat, I., Karnani, M.M., and Yuste, R. (2016). VIP+ interneurons control neocortical activity across brain states. J. Neurophysiol. 115, 3008–3017.

Jalbrzikowski, M., Jonas, R., Senturk, D., Patel, A., Chow, C., Green, M.F., and Bearden, C.E. (2013). Structural abnormalities in cortical volume, thickness, and surface area in 22q11.2 microdeletion syndrome: Relationship with psychotic symptoms. Neuroimage Clin. 3, 405–415.

Javitt, D.C. (2009). When doors of perception close: bottom-up models of disrupted cognition in schizophrenia. Annu. Rev. Clin. Psychol. 5, 249–275.

Javitt, D.C., and Freedman, R. (2015). Sensory processing dysfunction in the personal experience and neuronal machinery of schizophrenia. Am. J. Psychiatry 172, 17–31.

Ji, D., and Wilson, M.A. (2007). Coordinated memory replay in the visual cortex and hippocampus during sleep. Nat. Neurosci. 10, 100–107.

Kahn, R.S., and Keefe, R.S.E. (2013). Schizophrenia is a cognitive illness: time for a change in focus. JAMA Psychiatry 70, 1107–1112.

Karayiorgou, M., Simon, T.J., and Gogos, J.A. (2010). 22q11.2 microdeletions: linking DNA structural variation to brain dysfunction and schizophrenia. Nat. Rev. Neurosci. 11, 402–416.

Kargieman, L., Santana, N., Mengod, G., Celada, P., and Artigas, F. (2007). Antipsychotic drugs reverse the disruption in prefrontal cortex function produced by NMDA receptor blockade with phencyclidine. Proc. Natl. Acad. Sci. USA 104, 14843–14848.

Kocsis, B., Brown, R.E., McCarley, R.W., and Hajos, M. (2013). Impact of ketamine on neuronal network dynamics: translational modeling of schizophrenia-relevant deficits. CNS Neurosci. Ther. 19, 437–447.

Krystal, J.H., Karper, L.P., Seibyl, J.P., Freeman, G.K., Delaney, R., Bremner, J.D., Heninger, G.R., Bowers, M.B., Jr., and Charney, D.S. (1994). Subanesthetic effects of the noncompetitive NMDA antagonist, ketamine, in humans. Psychotomimetic, perceptual, cognitive, and neuroendocrine responses. Arch. Gen. Psychiatry 51, 199–214.

Lee, S.-H., Kwan, A.C., and Dan, Y. (2014). Interneuron subtypes and orientation tuning. Nature 508, E1–E2.

Lewis, D.A. (2014). Inhibitory neurons in human cortical circuits: substrate for cognitive dysfunction in schizophrenia. Curr. Opin. Neurobiol. 26, 22–26.

Lewis, D.A., Curley, A.A., Glausier, J.R., and Volk, D.W. (2012). Cortical parvalbumin interneurons and cognitive dysfunction in schizophrenia. Trends Neurosci. 35, 57–67.

Lo, C.-Y.Z., Su, T.-W., Huang, C.-C., Hung, C.-C., Chen, W.-L., Lan, T.-H., Lin, C.-P., and Bullmore, E.T. (2015). Randomization and resilience of brain functional networks as systems-level endophenotypes of schizophrenia. Proc. Natl. Acad. Sci. USA 112, 9123–9128.

Loftus, G.R., and Masson, M.E. (1994). Using confidence intervals in within-subject designs. Psychon. Bull. Rev. 1, 476–490.

Luczak, A., Barthó, P., and Harris, K.D. (2009). Spontaneous events outline the realm of possible sensory responses in neocortical populations. Neuron 62, 413–425.

Marshel, J.H., Garrett, M.E., Nauhaus, I., and Callaway, E.M. (2011). Functional specialization of seven mouse visual cortical areas. Neuron *72*, 1040–1054.

Mazurek, M., Kager, M., and Van Hooser, S.D. (2014). Robust quantification of orientation selectivity and direction selectivity. Front. Neural Circuits *8*, 92.

McNally, J.M., McCarley, R.W., and Brown, R.E. (2013). Chronic ketamine reduces the peak frequency of gamma oscillations in mouse prefrontal cortex ex vivo. Front. Psychiatry *4*, 106.

Miller, J.E., Ayzenshtat, I., Carrillo-Reid, L., and Yuste, R. (2014). Visual stimuli recruit intrinsically generated cortical ensembles. Proc. Natl. Acad. Sci. USA *111*, E4053–E4061.

Moran, L.V., and Hong, L.E. (2011). High vs low frequency neural oscillations in schizophrenia. Schizophr. Bull. *37*, 659–663.

Mukai, J., Tamura, M., Fénelon, K., Rosen, A.M., Spellman, T.J., Kang, R., MacDermott, A.B., Karayiorgou, M., Gordon, J.A., and Gogos, J.A. (2015). Molecular substrates of altered axonal growth and brain connectivity in a mouse model of schizophrenia. Neuron *86*, 680–695.

Niell, C.M., and Stryker, M.P. (2008). Highly selective receptive fields in mouse visual cortex. J. Neurosci. *28*, 7520–7536.

Niell, C.M., and Stryker, M.P. (2010). Modulation of visual responses by behavioral state in mouse visual cortex. Neuron *65*, 472–479.

Perdue, K.A., Green, K.Y., Copeland, M., Barron, E., Mandel, M., Faucette, L.J., Williams, E.M., Sosnovtsev, S.V., Elkins, W.R., and Ward, J.M. (2007). Naturally occurring murine norovirus infection in a large research institution. J. Am. Assoc. Lab. Anim. Sci. *46*, 39–45.

Perova, Z., Delevich, K., and Li, B. (2015). Depression of excitatory synapses onto parvalbumin interneurons in the medial prefrontal cortex in susceptibility to stress. J. Neurosci. *35*, 3201–3206.

Phoumthipphavong, V., Barthas, F., Hassett, S., and Kwan, A.C. (2016). Longitudinal effects of ketamine on dendritic architecture in vivo in the mouse medial frontal cortex. eNeuro *3*, ENEURO.0133-15.2016. http://dx.doi.org/10.1523/ENEURO.0133-15.2016.

Poels, E.M.P., Kegeles, L.S., Kantrowitz, J.T., Slifstein, M., Javitt, D.C., Lieberman, J.A., Abi-Dargham, A., and Girgis, R.R. (2014). Imaging glutamate in schizophrenia: review of findings and implications for drug discovery. Mol. Psychiatry *19*, 20–29.

Rolls, E.T., Loh, M., Deco, G., and Winterer, G. (2008). Computational models of schizophrenia and dopamine modulation in the prefrontal cortex. Nat. Rev. Neurosci. *9*, 696–709.

Roth, B.L. (2016). DREADDs for Neuroscientists. Neuron *89*, 683–694.

Scariati, E., Padula, M.C., Schaer, M., and Eliez, S. (2016). Long-range dysconnectivity in frontal and midline structures is associated to psychosis in 22q11.2 deletion syndrome. J Neural Transm (Vienna) *123*, 823–839.

Schneider, C.A., Rasband, W.S., and Eliceiri, K.W. (2012). NIH Image to ImageJ: 25 years of image analysis. Nat. Methods *9*, 671–675.

Sigurdsson, T., Stark, K.L., Karayiorgou, M., Gogos, J.A., and Gordon, J.A. (2010). Impaired hippocampal-prefrontal synchrony in a genetic mouse model of schizophrenia. Nature *464*, 763–767.

Sippy, T., and Yuste, R. (2013). Decorrelating action of inhibition in neocortical networks. J. Neurosci. *33*, 9813–9830.

Smetters, D., Majewska, A., and Yuste, R. (1999). Detecting action potentials in neuronal populations with calcium imaging. Methods *18*, 215–221.

Sohal, V.S., Zhang, F., Yizhar, O., and Deisseroth, K. (2009). Parvalbumin neurons and gamma rhythms enhance cortical circuit performance. Nature *459*, 698–702.

Spencer, K.M., Nestor, P.G., Perlmutter, R., Niznikiewicz, M.A., Klump, M.C., Frumin, M., Shenton, M.E., and McCarley, R.W. (2004). Neural synchrony indexes disordered perception and cognition in schizophrenia. Proc. Natl. Acad. Sci. USA *101*, 17288–17293.

Stark, K.L., Xu, B., Bagchi, A., Lai, W.-S., Liu, H., Hsu, R., Wan, X., Pavlidis, P., Mills, A.A., Karayiorgou, M., and Gogos, J.A. (2008). Altered brain microRNA biogenesis contributes to phenotypic deficits in a 22q11-deletion mouse model. Nat. Genet. *40*, 751–760.

Stosiek, C., Garaschuk, O., Holthoff, K., and Konnerth, A. (2003). In vivo two-photon calcium imaging of neuronal networks. Proc. Natl. Acad. Sci. USA *100*, 7319–7324.

Sullivan, E.M., Timi, P., Hong, L.E., and O'Donnell, P. (2015). Reverse translation of clinical electrophysiological biomarkers in behaving rodents under acute and chronic NMDA receptor antagonism. Neuropsychopharmacology *40*, 719–727.

Uhlhaas, P.J., and Singer, W. (2010). Abnormal neural oscillations and synchrony in schizophrenia. Nat. Rev. Neurosci. *11*, 100–113.

Venables, N.C., Bernat, E.M., and Sponheim, S.R. (2009). Genetic and disorder-specific aspects of resting state EEG abnormalities in schizophrenia. Schizophr. Bull. *35*, 826–839.

Vinck, M., Batista-Brito, R., Knoblich, U., and Cardin, J.A. (2015). Arousal and locomotion make distinct contributions to cortical activity patterns and visual encoding. Neuron *86*, 740–754.

Walterfang, M., McGuire, P.K., Yung, A.R., Phillips, L.J., Velakoulis, D., Wood, S.J., Suckling, J., Bullmore, E.T., Brewer, W., Soulsby, B., et al. (2008). White matter volume changes in people who develop psychosis. Br. J. Psychiatry *193*, 210–215.

Wang, X.-J., and Krystal, J.H. (2014). Computational psychiatry. Neuron *84*, 638–654.

Whitfield-Gabrieli, S., and Ford, J.M. (2012). Default mode network activity and connectivity in psychopathology. Annu. Rev. Clin. Psychol. *8*, 49–76.

Yan, M., and Ye, K. (2007). Determining the number of clusters using the weighted gap statistic. Biometrics *63*, 1031–1037.

Yang, G., Pan, F., Parkhurst, C.N., Grutzendler, J., and Gan, W.-B. (2010). Thinned-skull cranial window technique for long-term imaging of the cortex in live mice. Nat. Protoc. *5*, 201–208.

Yang, G.J., Murray, J.D., Repovs, G., Cole, M.W., Savic, A., Glasser, M.F., Pittenger, C., Krystal, J.H., Wang, X.-J., Pearlson, G.D., et al. (2014). Altered global brain signal in schizophrenia. Proc. Natl. Acad. Sci. USA *111*, 7438–7443.

Yuste, R. (2015). From the neuron doctrine to neural networks. Nat. Rev. Neurosci. *16*, 487–497.

Yuste, R., and Katz, L.C. (1991). Control of postsynaptic Ca2+ influx in developing neocortex by excitatory and inhibitory neurotransmitters. Neuron *6*, 333–344.

Zhu, J., Zhuo, C., Liu, F., Qin, W., Xu, L., and Yu, C. (2016). Distinct disruptions of resting-state functional brain networks in familial and sporadic schizophrenia. Sci. Rep. *6*, 23577.

STAR★METHODS

KEY RESOURCES TABLE

REAGENT or RESOURCE	SOURCE	IDENTIFIER
Chemicals, Peptides, and Recombinant Proteins		
Ketamine HCL	Pfizer	Cat#:NADA 45-290
Clozapine N-Oxide	Enzo Life Sciences	Cat#:BML-NS105-0025
Experimental Models: Organisms/Strains		
Mouse: Pvalb$^{tm1(cre)Arbr}$	The Jackson Laboratory	Cat#:008069
Mouse: *Df(16)A$^{+/-}$ and +/+ wildtype littermates*	J.A. Gogos; Stark et al., 2008	RRID: MGI_3802827
Mouse: Ai14; B6.Cg-Gt(ROSA)26Sor$^{tm14(CAG-tdTomato)Hze/J}$	The Jackson Laboratory	Cat#:007914
Oligonucleotides		
Primers for Df16 deletion: 5′- ATTCCCCATGGACTA ATTATGGACAGG-3′ and 5′ GGTATCTCCATAAGAC AGAATGCTATGC 3′	This paper	N/A
Primers for control band: 5′ CTAGGCCACAGAATTGAA AGATCT 3′and 5′GGTGGAAATTCTAGCATCATCC 3′	This paper	N/A
Recombinant DNA		
AAV1.Syn.GCaMP6s.WPRE.SV40	Chen et al., 2013; Penn Vector Core	Cat#:AV-1-PV2824
AAV1.Syn.GCaMP6f.WPRE.SV40	Chen et al., 2013; Penn Vector Core	Cat#:AV-1-PV2822
AAV5-hSyn-DIO-hM4D(Gi)-mCherry	Roth, 2016; UNC Vector Core	Cat#:44362-AAV5
Software and Algorithms		
ImageJ 1.47v	Schneider et al., 2012	https://imagej.nih.gov/ij/download.html
MOCO (for ImageJ)	Dubbs et al., 2016	http://www.columbia.edu/cu/biology/faculty/yuste/Methods/moco.zip
MATLAB 2015b	MathWorks	https://www.mathworks.com/
MATLAB codes	This paper	hamm.jordan@gmail.com
MassHunter v 3.1	Agilent Technologies	http://www.agilent.com/
Prairie view 5.3	Bruker Corporation	https://www.bruker.com
Axon Multiclamp Commander	Molecular Devices	http://mdc.custhelp.com/app/
Other		
UMP3 microsyringe pump	World Precision Instruments	Model # SYS-MICRO4
Osmotic minipump	Alzet	Model # 2001
Agilent 1290 Infinity UHPLC	Agilent Technologies	Model # G4220-90301
Custom build Ultima In Vivo two-photon microscope	Bruker Corporation	Model: U-IV-02
Tunable Ti:Sapphire laser	Coherent	Model: Chameleon Ultra II
Pockels cell	Conoptics	Model # 350-160BK
Pockels cell driver	Conoptics	Model # 302 RM
16-channel multielectrode Probe	Neuronexus Technologies	Model # a1x16-3mm 50-177
MultiClamp 700B amplifier	Molecular Devices	Model # 2500-0157
Plexon MiniDigi digitizing amplifier	Plexon	Model # 94211
PLX-4 System Controller	Plexon	Model # 80001

CONTACT FOR REAGENT AND RESOURCE SHARING

Further information and requests for resources and reagents should be directed to and will be fulfilled by the Lead Contact, Dr. Jordan Hamm (jph2164@columbia.edu or hamm.jordan@gmail.com).

EXPERIMENTAL MODEL AND SUBJECT DETAILS

All experimental procedures were approved by the Columbia University Institutional Animal Care and Use Committee (IACUC) and carried out in accordance with Columbia University institutional animal care guidelines. Chronic ketamine (KET) or saline (SAL) experiments were performed on adult parvalbumin-Cre or parvalbumin-Cre × LSL-tdTomato transgenic mice, obtained from The Jackson Laboratory (from a C57BL/6 background, 22-32 g), at the age of postnatal day (P) P60-P110 (first recording day). $Df(16)A^{+/-}$ mice (RRID: MGI_3802827) and their wild-type, homozygous littermates/cagemates (WT; P80-P130, 22-32 g) were generated on a C57BL/6J background (Stark et al., 2008). All animals were ketamine naive at the start of testing and were not used for previous or subsequent experimentation. Calcium imaging data are reported on 7 SAL (2 female, 4 PV-cre, 3 PV-cre;;td:tomato), 7 KET mice (2 female, 3 PV-cre, 4 PV-cre;;td:tomato), 7 $Df(16)A^{+/-}$ mice (all male), and 7 WT (all male). LFP data are reported on 7 SAL and 6 KET treated mice (all PV-cre), and 8 $Df(16)A^{+/-}$ and 5 WT (all male). Group type was randomly assigned (in pairs for KET/SAL experiments) and blind to the experimenter/analyst throughout experiments, data processing, and analysis. Mice were housed in Allentown ventilated rack caging (IVCs cages) with 1 to 3 cagemates of the same sex on a 12 hr light/dark cycle, and were fed Purina Lab Diet 5053. Sentinel mice tested negative on all major pathogens tested (14 viruses, M. pulmonis, endo/ecto parasites) except murine norovirus (7/8 tested positive; MNV). MNV is by far the most common infectious agent in laboratory mice and is typically asymptomatic (Perdue et al., 2007).

METHOD DETAILS

Animals, Surgery, and Training

Virus injection, head plate fixation, skull thinning, and minipump implantation (KET/SAL only) were carried out in that order over the course of 5 weeks. In the first surgery (virus injection), 3-4 weeks prior to the first imaging session, mice were anesthetized with isoflurane (initially 3% (partial pressure in air) and reduced to 1%–2%). A small window was made through the skull above left V1 using a dental drill (coordinates from lambda: X = −250, Y = 20 μm) taking care not to pierce the dura mater. A glass capillary pulled to a sharp micropipette was advanced with the stereotaxic instrument, and 750nl solution of 1:1 diluted AAV1.Syn.GCaMP6f.WPRE.SV40 (3 KET, 2 SAL) or AAV1.Syn.GCaMP6s.WPRE.SV40 (all other mice; obtained from the University of Pennsylvania Vector Core) was injected into putative layer 2/3 over a 5 min period at a depth of 200-300 μm from the pial surface using a UMP3 microsyringe pump (World Precision Instruments).

Approximately 3 weeks after virus injection, mice were anesthetized as previously described and a titanium head plate was attached to the skull centered around the virus injection site using dental cement (Miller et al., 2014). Mice were allowed to recover for at least 5 days in their home cage. In this time, mice were given analgesics (5mg/kg carprofen I.P.) and accustomed to experimenter handling, including brief head-restraint periods, until mice showed non-stressed behavior, which usually began on the second day. Mice then underwent training to maneuver with their head fixed approximately 1 inch above a rotating wheel, beginning with a 30 min session. This progressed until mice could distribute weight on the wheel evenly and appeared calm (grooming, locomotion) and without signs of distress (tremors, freezing, etc), which generally occurred after the first session (Miller et al., 2014). During training sessions and prior to the first imaging session, mice viewed moving square-wave gratings (see below) for stimulus habituation.

On the first day of imaging, mice were anesthetized again with isoflurane and a small circle (approximately 1 mm in diameter) was thinned with a dental over the left V1 centered just anterior to the injection site or removed (for LFP experiments). The skull was thinned until the bone, moistened with saline, was transparent enough so that the underlying vasculature was visible to the naked eye (usually 20 min of drilling). The thin skull preparation prevents exposure of the cortex and meninges and is a minimally invasive method for chronic imaging of cortical changes (Yang et al., 2010). The mouse was then allowed to wake up and was transferred to the wheel. After approximately one hour, imaging began. After the first imaging session, mice were returned to their home cage (SAL/KET) or sacrificed (Df(16)A$^{+/-}$/WT). The following day, (for SAL/KET) an osmotic minipump was implanted subcutaneously (Alzet, model 2001) which released approximately 60 mg/kg/day ketamine HCL (KET mice) or an equivalent volume of saline (SAL mice) at 1.0 μl per hour for 7 days. This dose is within the previous range suggested for mouse chronic ketamine models (Behrens et al., 2007; Chatterjee et al., 2012). The pump was weighed before and after filling to ensure the absence of air bubbles (per manufacturer's instructions).

To estimate plasma levels of ketamine achieved during this procedure, KET mice were sacrificed at day 4 blood was harvested from a cardiac puncture, centrifuged at 2000 cycles per second at 4C, and the supernatant serum was stored at −20 C. Ketamine in the serum samples was extracted using liquid –liquid extraction and quantitated using liquid chromatography-tandem mass spectrometry (LCMS/MS) using platform comprising Agilent 6410 triple quad mass spectrometer coupled with Agilent 1290 Infinity UHPLC (Agilent Technologies) controlled by MassHunter v 3.1 (Agilent Technologies, Santa Clara, CA). Average plasma levels of ketamine were 135.1 ng/ml (range 129.8-142.4), a concentration at the low end of acute ketamine induced psychotic brain states in human studies (Driesen et al., 2013). As expected, saline treated mice (n = 3) did not express detectable levels of ketamine (< 2.50 ng/ml). The second imaging day took place one week after implantation of the minipump. Skull thinning was repeated if necessary (about 20% of the time). Animals were sacrificed shortly after the final imaging session, and pumps were removed and inspected to ensure the absence of perforation or clogging.

Genotyping of *Df(16)A*$^{+/-}$ mice

Df(16)A$^{+/-}$ were acquired from a colony maintained by the Gogos lab (Stark et al., 2008). Mice were genotyped twice from tail samples (stored at $-20C$ for less than 2 weeks) collected before and after experimentation. Samples were screened for the presence of the deficiency (Df(16)A) by using the primers: 5′- ATTCCCCATGGACTAATTATGGACAGG-3′ and 5′ GGTATCTCCATAAGACAGAATG CTATGC 3′, which amplify an 829 basepair band. Primers 5′ CTAGGCCACAGAATTGAAAGATCT 3′and 5′GGTGGAAATTC TAGCATCATCC 3′ amplify a 324 bp internal control band. PCR cycling conditions we used were: 94°C for 3 min; 35 cycles of 94°C for 30 s, 60°C for 1min, and 72°C for 1 min; 72°C for 10 min.

Two-Photon Calcium Imaging

The activity of cortical neurons was recorded by imaging fluorescence changes under a two-photon microscope (Bruker Ultima In Vivo; Billerica, MA) excited with a Ti:Sapphire laser (Chameleon Ultra II; Coherent) tuned to 940 nm. The laser beam was intensity modulated with a Pockels cell (Conoptics 350-160BK, with 302 RM driver) and scanned with galvometers through a 20 × 0.9 N.A.; (Olympus) water immersion objective (Figures 2A and 2B). To ensure stability of the imaging meniscus for long duration imaging sessions, a small volume (approx. 1ml) of Aquasonic ultrasound gel (Parker Laboratories) was centrifuged and dolloped onto a moistened, thinned skull. Scanning and image acquisition were controlled by Prairie View software (3.395 frames per second for 256 × 256 pixels, 1.6 microsecond dwell time per pixel, 200-225 um beneath the pial surface). The Pockels cell blanked the laser outside the imaging field to minimize laser exposure. On both imaging days (before and after treatment) mice were allowed 1 hr on the wheel before imaging began. Imaging consisted of a visual stimulation condition (15 min), followed by 20-40 min of awake rest in a dark room with the monitor off, followed by a second visual stimulation. Rest sessions were not collected for 1 SAL and 1 KET mouse. Sessions started at the same time of day for both sessions within a mouse (starting between 11am and 4pm). Mice and recordings (LFP, locomotion) were visually monitored by the experimenter to ensure they were awake during data collection. On week 1, at the end of the session, an imaging dataset was recorded in which the field of view was slowly moved systematically in 3 dimensions, thoroughly surveying the cortical area where our calcium indicator was expressed. This movie helped in locating the same cortical region on week 2 (using mainly vasculature landmarks as a guide; e.g., Figures S2A and S2C). Locomotion was recorded with an infared LED/photodarlington pair (Honeywell S&C HOA1877-003), which consists of a small c-shaped device positioned at the edge of the rotating wheel (striped with black tape) connected to the imaging computer as an analog input. Locomotion was detected as voltage detections in the photodarlington readout. While previous work has suggested that locomotion enhances visual processing in V1 in mice (Niell and Stryker, 2010), most of our mice did not exhibit enough locomotion to enable thorough examination of this effect in our chronic models (< 10% of frames). Therefore, when detected, frames or trials during locomotion periods were excluded along with the previous and subsequent 12 frames; this did not change the pattern of effects.

Visual Stimulation

Visual stimuli were generated using the Psychophysics Toolbox in MATLAB (MathWorks) and displayed on a liquid crystal display monitor (19-inch diameter, 60-Hz refresh rate) positioned 15 cm from the right eye, roughly at 45° to the long axis of the animal. Stimuli were full-field squarewave gratings (100% contrast, 0.04 cycles per degree, 2 cycles per second) drifting in twelve different directions in random order presented for 3 s, followed by an interstimulus interval of 7-8 s of mean luminescence gray screen (Figure S2E). In each session, mice saw a total of 15 presentations of each stimulus. The timing and identity of gratings played in MATLAB were synchronized with image acquisition by outputting an analog voltage trigger synchronized with stimulus onset and offset and recorded with the imaging computer using Prairie View 5.2 software (Bruker; Billerica, MA). The timing between actual stimulus onset and recorded voltage traces in Prairie View was confirmed beforehand using a photodiode sensor with a reverse biased voltage output recorded by the software in tandem with the MATLAB output triggers.

Local Field Potential recordings

Local field potentials (LFPs) were recorded as previously reported in our lab (Hamm and Yuste, 2016), using mice that did not undergo virus injection or skull thinning described above. Recordings occurred in *Df(16)A*$^{+/-}$ and WT mice or in SAL/KET treated mice only *after* treatment due to the invasiveness of intracortical LFPs. On the day of recording a small craniotomy was made (less than 1 mm^2). LFPs were either recorded with a single AgCl- electrode in a glass pipette filled with saline solution or a single contact from a 16 channel linear silicon probe (spaced at 50 Um intervals; model a1x16-3mm 50-177, Neuronexus Technologies, Ann Arbor MI) inserted perpendicular to and with the top electrode aligned just at the pial surface (visually confirmed with an adjustable miniature digital microscope; Adafruit (New York, NY)). Recordings were made from approximately 250um below the pial surface. Recordings were referenced to the skull above prefrontal cortex and grounded to the headplate. Continuous data were acquired with either a MultiClamp 700B amplifier/software (Molecular Devices, Sunnyvale, CA) or a Plexon MiniDigi amplifier and software (Plexon, Dallas, TX) and analog filtered from 0.1 Hz to 10 kHz. Mice viewed visual stimuli (described above) of either 1 or 3 s in duration. LFP data were manually prescreened for excessive artifact (e.g., signal greater than 8 standard deviations) and deviant trials were removed. Trials during locomotion were also excluded (a total of < 10% of trials). Data were then digitally filtered from 0.5 to 300Hz (bandpass least-squares FIR) and with a 60Hz notch filter.

Acute ketamine and pharmacogenetic suppression of PVs

As described above, an additional set of adult parvalbumin-Cre mice were injected with both GCaMP6s and AAV5hsynDIOhM4D(Gi)mCherry (UNC vector core), and underwent headplate implantation, head-fixation training, and imaging (n = 7, n = 5 GCaMP6 only controls). The efficacy of our methods in successfully targeting PVs have been previously verified in our lab with mCherry and PV immunohistochemistry (Hamm and Yuste, 2016; Jackson et al., 2016; Sippy and Yuste, 2013). On the day of recording, mice ambulated on a treadmill in a dark room as described above while images were recorded at approximately 4 Hz. Then mice each received a subcutaneous injection of Clozapine N-Oxide (12 mg/kg; Hamm and Yuste, 2016; Perova et al., 2015), followed by a second set of images recorded starting 30 min later. For testing of the effects of acute ketamine, adult Pv-Cre mice (n = 3) or wild-type (n = 4) underwent a similar set of procedures as CNO injected mice except three recording sessions were acquired, each 30 min post-injection and lasting at least 20 min: baseline, post-saline injection (subcutaneous), and post-ketamine injection (15mg/kg, subcutaneous; equivalent volumes used for SAL and KET).

Study of Parvalbumin-containing Interneurons

Using transgenic mice expressing cre-recombinase selectively in PVs (PV-cre) crossed with cre-reporting mice expressing the florescent protein td-Tomato (Ai14; B6.Cg-Gt(ROSA)26Sor$^{tm14(CAG-tdTomato)Hze/J}$), PVs were identified in a subset of mice (PVcre:: tdTomato) by somatic co-localization of GCaMP6s and tdTomato (Figure S7A; 22 PVs across 3 SAL mice; 34 PVs across 4 KET mice; average of 4 neurons per imaged population) (Hofer et al., 2011; Miller et al., 2014). Cells co-expressing tdTomato and GCaMP6s were identified with two-photon stimulation at 940 nm or 1010 nm and using 2 PMTs filtered for green (510/20 nm) and red (607/45); we typically identified 2 to 4 per mouse (at max 8, always less than 8%; Figure S7). Florescent traces from PV ROIs were identified and processed similarly to non-PVs with regard to pixel selection and halo subtraction (see above). Two-photon imaging measured calcium dynamics in PVs are known to differ substantially from pyramidal neurons, with longer decays and more ongoing fluctuation (Hofer et al., 2011). This may be partially due, among other differences, to the higher baseline firing rates and calcium buffering dynamics of PVs. In the present study, we focused on PV calcium dynamics i) evoked by visual stimuli and ii) locked to statistically defined "ensemble activations" (or high activity states of the network).

QUANTIFICATION AND STATISTICAL ANALYSIS

Depending on the question addressed, analyses focused on cell averages (e.g., activity levels, orientation tuning, correlation coefficients) or mouse-wise averages (LFP measures, locomotion, proportion of significant correlation pairs, ensemble/network-level), from 6-7 mice for each condition per set of experiments (e.g., chronic saline versus ketamine). This report contains no independent replications of any set of experiments. Statistical tests for each experimental condition is described in the following sections and include paired t tests, independent t tests, one-way ANOVAs, repeated-measures ANOVAs, and mixed ANOVAs (between and within subject factors). As clarified in figure legends, error bars reflect standard errors of the mean (SEM), but, when statistical comparisons were mixed ANOVA, repeated-measures ANOVA, or paired t tests, standard error bars reflect within-subjects/within-cells standard error (Loftus and Masson, 1994).

Spectral analysis of LFP

Baseline LFP power was measured in 2 s windows (0.5 Hz resolution) between and after visual stimulations. A Fast-Fourier transform (FFT) was carried out, and the spectral power (squared absolute value of the complex output of the FFT) was averaged across all time windows, divided (relative; Figures S1C and S1D) or not divided (absolute; Figures 1A and 1E) by the broadband power across frequencies from 1 to 120 Hz, and then multiplied by the frequency (for rescaling for visual presentation only, i.e., correcting for 1/f component).

For analysis of stimulus elicited oscillatory dynamics, LFP data from single trials were segregated into bins −2000ms pre to 5000ms post grating stimulus onset. Data were convolved with a family of modified morlet wavelets from ranging from 2 to 120Hz in 2Hz and 20ms steps with wavelet size increasing linearly from 1 to 20 cycles using code written in MATLAB and EEGLAB 9.0 (Delorme and Makeig, 2004). This approach is ideal for time varying analysis of oscillatory dynamics since it optimizes effective frequency resolution at low frequencies and time resolution at higher frequencies (Hamm et al., 2012). Oscillatory power was expressed in decibels and was averaged over trials. Average power values for each frequency in the baseline period (−1000ms to −100ms pre-grating onset) were subtracted to yield a single time-frequency evoked spectra for each mouse (Figures 1D and 1H).

Statistical comparisons focused on frequency bins derived via principal components analysis (Hamm and Yuste, 2016; Hamm et al., 2014). Trial averaged time-frequency spectra (including baseline) were converted to z-scores for each mouse, and concatenated in time across all mice. A scree plot indicated that 5 components were present. After varimax rotation, the final frequency bins were 1-14Hz (low/theta/alpha), 15-34 Hz (beta), 35-58 Hz (gamma1; excluding 59-61 Hz), 62-110 Hz (gamma2), and > 111Hz (high frequency; excluding 119-121 Hz), highly consistent with traditionally demarcated bin boundaries (Buzsaki, 2009). Baseline absolute power spectra were compared between SAL/KET and Df(16)A$^{+/−}$/WT with 2 sample t tests (df = 11) for each frequency band. Stimulus elicited power was averaged across the first 500ms post-grating onset (since this was when the majority of the response was present) for each bin. Two sample t tests (df = 11) were applied for each frequency band, (comparing between SAL/KET and Df(16)A$^{+/−}$/WT).

Phase locking (or inter trial phase coherence) assess the consistency of the stimulus elicited LFP waveform without regard to amplitude variations. It is calculated by dividing the complex result of the wavelet analysis by its absolute value for every frequency and time point (and normalized for number of trials as previously described; Hamm et al., 2012). Statistical comparisons were carried out in the same manner as for spectral power, except focusing the first 150 ms where the response is maximal.

For all oscillatory measures, two-tailed significance was used, but trend-level effects were reported since LFP experiments had an a priori directional hypothesis based on the schizophrenia literature (SZ > H for baseline; H > SZ for stimulus evoked; Hamm et al., 2014; Uhlhaas and Singer, 2010).

Image Analysis

Imaging datasets were scored similarly to previous reports (Chen et al., 2013; Hamm and Yuste, 2016). The raw images were processed to correct translational brain motion artifacts using the MOCO algorithm and plugin (Dubbs et al., 2016) written in house for ImageJ (Schneider et al., 2012). Then, cell regions of interest (ROIs) were detected semi-automatically for each imaging session and individually confirmed as follows. Mean, standard deviation, and std × skewness projections (pixel-wise) were calculated across all imaging frames (roughly 14000-25000) and plotted for reference (Figure S3A). Then, rectangular sections were selected around the apparent cell bodies using a GUI created in MATLAB. A principal components analysis (PCA) was computed on the pixels contained within the sections, and the pixels with weights at least 80% of the maximum of the first PCA component were defined as the ROI and spatially plotted (Figure S3B) along with the florescence trace averaged across these pixels (e.g., Figure S3C, top). Cells with faint, sparse (< 5 events across both weeks), or largely atypical calcium transients were excluded from further analysis at this step (< 20%; cells not showing periods of low florescence with intermittent sharp peaks; e.g., Figure S3; Chen et al., 2013). In general, these criteria focused analyses on cells with a bursting profile and firing rate typical of layer 2/3 neocortical neurons (Pyramidal and non-PV pyramidal neurons). PVs, for example, which have higher baseline activity and ostensibly different calcium indicator dynamics (Hofer et al., 2011) were likely excluded at this step, and, when possible (using mice with florescent indicator tdTomato tagged to PVs), we were able directly confirm these differences and exclude PVs from network analyses (Figure S7). This exclusion did not substantively affect the main results (e.g., ensemble reliability $F^{interaction}(1,10) = 4.98$, $p < .05$ without PVs; $F^{interaction}(1,10) = 5.14$, $p < .05$ with PVs). The average number of active cells used for further analyses did not differ between conditions within experiments (mean/range; SALpre = 74 (52/93); SALpost = 79 (53/100); KETpre = 75 (53/100); KETpost = 73 (45/120); $F^{interaction}(1,12) = 0.58$, $p = 0.28$; $F^{group}(1,12) = 0.14$, $p = 0.71$; WT$^{+/-}$ = 66 (31/101); Df(16)A$^{+/-}$ = 51 (25/85); $F(1,12) = 1.65$, $p = 0.22$). Florescence of active cells was then calculated as the average across all pixels within this ROI minus the average of the pixels just outside the selected rectangle, termed the "halo," which excluded pixels from nearby cell bodies (Figure S3C). This subtraction removed background contamination from neuropil and nearby cells. Completing this step ensures maximal correspondence between florescence and actual cell spiking (Chen et al., 2013). The remaining traces were then filtered with a 3 s *lowess* envelope (Hamm and Yuste, 2016), a regression based smoothing approach which is tolerant of sharply changing values on the edges of the window. Finally, the first discrete derivative was scored either as Δf (within cell/single cell comparisons), or as within-cell maximum normalized Δf (population analyses).

Single cell analyses

For each neuron recorded, we estimated events using thresholds set as 3.1 standard deviations ($p < .001$) above baseline Δf for each neuron (lower 8% of values; Carrillo-Reid et al., 2015; Hamm and Yuste, 2016). We first quantified overall activity levels as the proportion of frames during which a neuron was "active" (i.e., displaying an event). Events/active frames were automatically marked as time frames with Δf values which exceeded thresholds. Single calcium events normally consist of multiple closely co-occurring action potentials, or "bursts." For scaling consistency across experiments and conditions and to account for baseline differences across mice, we divided activity levels for each neuron by the mouse-wise average from week 1 only (SAL/KET), or by the global average from WT mice (22q11.2 model). This procedure did not change the pattern of results (i.e., KET still showed an increase when using raw values $F^{ket}(872) = 5.76$, $p < .05$; means/std; KET^{pre} = 2.8% active frames/1.7; KET^{post} = 3.1/1.7; WT = 2.6/1.2; Df(16)A$^{+/-}$ = 2.5/1.1). For SAL/KET experiments, activity level comparisons were carried out with a 2-by-2 mixed ANOVA on individual cells with TREATMENT as the between subject variable and WEEK as the within subject variable. Follow-up one-way ANOVAs were carried out separately for KET and SAL to interpret interactions. For Df(16)A$^{+/-}$ experiments, a single one-way ANOVA was carried out on activity levels.

In order to understand the nature of this change in KET, we focused on neurons identifiable pre and post SAL/KET treatment (Figures S2 and S4; 4 SAL, 5 KET). Week 2 sessions in which a substantial number of cells (> 10) from week 1 could be located precisely, cells were visually matched between weeks by 2 independent scorers for subsequent comparisons. Since the GCaMP6 series has near zero basal florescence, this was a difficult task to do with certainty during the imaging session, and had to be performed post hoc using z-projection plots (see Figure S3). Only regions of interest with agreement between the 2 scorers were counted as the same cell. The average overall activity level (average Δf over all frames), event maximum, and event frequency (contiguous active frame blocks, or "events," per minute) were quantified for each cell and condition. Again, values were normalized within each mouse using the week-1 event size and event rate, and the same statistical procedures were repeated.

Differences in single neuron disinhibition was one principal difference found between our pharmacological and genetic models. One potential confound is that only the KET/SAL experiments included female mice (n = 4; 2 each) and GCaMP6f (n = 5; 3 KET, 2 SAL), while the genetic model experiments were on only males and with only GCaMP6s, but additional analyses refute this

possibility. First, excluding females from the KET/SAL analysis did not change the effects ($F^{interaction}(1,1382) = 4.79$, $p < .05$; $F^{KET}(765) = 5.61$, $p < .05$; $F^{SAL}(617) = 0.54$, $p = 0.46$; n = 5 mice KET, 767 cells; n = 5 mice SAL, 619 cells). Second, while GCaMP6f has a much shorter decay time than GCaMP6s, our analyses focused only on the rise magnitudes/times (increases in florescence) and were therefore less likely affected by this experimental difference. The data concur with this hypothesis, since excluding GCaMP6f mice from an alternative analyses show that KET still showed disinhibition of ongoing activity ($F^{interaction}(1,1060) = 6.11$, $p < .05$; $F^{KET}(468) = 7.89$, $p < .01$; $F^{SAL}(892) = 0.43$, $p = 0.50$; n = 4 mice KET, 470 cells; n = 5 mice SAL, 619 cells).

Pairwise analysis

Pairwise coactivity (or functional connectivity) between single cells was assessed by calculating similarity values between cell pairs. For each cell, the Δf value across all frames was vectorized in n-dimensional space (where n = number of frames). The similarity of each cell/vector pair (Ca, Cb) was calculated as the angle between the vectors in n-dimensional space, or the normalized inner-product (Carrillo-Reid et al., 2015):

$$\text{S-index}^{Ca,Cb} = C_a \cdot C_b \Big/ \left(\left(|C_a|^2 + |C_b|^2 \right) \Big/ 2 \right).$$

This metric is bound between 0 and 1 (1 meaning that activity across time points is completely identical between cells) and is similar to cosine similarity with the added provision that cell pairs with similar relative magnitudes will have higher values than those with differing relative magnitudes, a step not necessary when cell activities are binary. This similarity metric was chosen to assess cell-cell correlations instead of more traditional methods (e.g., Pearson correlation) since calcium transients (rises in florescence) are relatively sparse (approx. 3% of frames on average) do not show negative values. Detecting a difference between an absence of coactivation between cells (0 correlation) and an inhibitory relationship (negative correlation) would prove difficult to interpret directly. Thus high cell-cell similarities represented high coactivation probabilities between cells across up-states, and low values represented a lack thereof. Since wide distributions of similarity values were observed, and could vary depending on the activity level and the duration of recording, we first sought, within each network, to determine what a "significant" amount of pairwise synchrony was with a bootstrapping procedure. Individual cell time courses were shifted by random amounts in time separately for each cell (holding individual cell activity levels constant at each step) and average pairwise synchrony values were calculated for all cells in these surrogate datasets. This step was repeated 10000 times (Cossart et al., 2003), creating a distribution of similarity indices expected at chance level for each cell pair. Cutoffs were set at the 99th percentile of the random distributions. For each mouse, we determined the proportion of cell pairs greater than this cutoff, and compared these proportions with a 2-by-2 mixed ANOVA on mice with TREATMENT as the between subject variable and WEEK as the within subject variable. Follow-up one-way RM ANOVAs were carried out separately for KET and SAL to interpret interactions. For Df(16)A$^{+/-}$ experiments, a single one-way ANOVA was carried out. As we observed obvious changes in the distribution peaks despite no change at the tails (Figures 2I and 2M), we additionally compared the means of all cell-pairs across all mice with the same statistical approach. Importantly, while traditional tests of distribution differences (e.g., Kolmogorov–Smirnov or Cramer-von Mises tests) both confirmed that KET and Df(16)A+/− pairwise coactivity distributions were deviant, these tests were overpowered in this experiment and were excluded. Even the SAL model, which ostensibly exhibited nearly identical distributions before and after treatments (Figure 2E), elicited a significant effect in both K-S and C-M tests.

Population analysis

Population level analyses of ongoing activity focused on the state similarity of cortical "ensemble" activations, or time-frames with significant levels of coactivity. First, a bootstrap approach was carried out on individual datasets in order to determine what characterized an ensemble as opposed to momentarily high activity states occurring due to uncorrelated variation in firing rates across cells. Δf values were normalized within cells by dividing all values by their maximum Δf across all recorded frames (Figure S5A). Δf values across all cells were then averaged within each frame (Figure S5B), yielding a value for each frame which is bound between 0 and 1, and represents the percentage of total possible network activity (e.g., 0.12 = 12% inferred activity ceiling). Importantly, the relative amount of network-wide coactivity did not differ between conditions (Figures S6A–S6C). Individual cell time courses were then shifted by random amounts in time separately for each cell (holding individual cell activity levels constant at each step) and average network activity values were calculated for all frames in these surrogate datasets. This step was repeated 10000 times (Cossart et al., 2003), creating a distribution of network activity magnitudes expected at chance level (Figure S5C). Cutoffs were set at the 99th percentile of the random distributions, which determined that the global "ensemble" definition (i.e., when combining all 38 datasets) was 0.06 or 6% of ceiling. We determined cutoffs on individual datasets, assigning instantaneous "peak" activity frames (local maxima in Figure S5B separated by at least 1.5 s) which exceeded thresholds as "ensemble activations." Focusing only on peaks served to exclude the similarity shared by adjacent frames. Each dataset exhibited between 150 and 250 significant ensembles activations during the first 20 min ongoing activity, so we focused further analyses on just the highest 150 peaks from each dataset.

The next step was to determine which ensemble activations showed population level patterns of activation which repeated, or had similarity values with subsequent ensemble activity above chance values, suggesting recurrent ensembles or attractor states in the ongoing activity. We calculated between frame "similarity index" as described above on frame-frame pairs (instead of cell-cell activity patterns), yielding 150 by 150 similarity matrices for each mouse (Figures 3B and S5D). We then used a bootstrap method again

to determine what constitutes ensemble repeats (Figure S5E), using within-frame shuffling 10000 times, holding overall activity levels constant. The global significant similarity value across all ensemble activity was S.I. = 0.47, p < .01. Individually derived S.I. cutoffs were derived for each mouse, for each week (when applicable), and used to i) re-adjust histograms for group-wise plotting (Figures 3I–3K) and ii) to determine the proportion of significant ensemble repeats, which was between 15% and 25% of frames on average, (15-25 times more likely than chance). The proportion of ensemble repeats for each mouse was compared with the same ANOVA models as described for pairwise comparisons.

Next ongoing data from ensemble activation frames was factorized with Principal Components Analysis (P.C.A; cells as variables) to i) demonstrate that a variety of network patterns were present in the ongoing activity (Carrillo-Reid et al., 2015; Miller et al., 2014) rather than simply one repeated high activity state (Figures 3A, S6D, and S6E), and ii) further confirm that KET reduced overall activity pattern fidelity across time rather than simply increasing the number of distinct states present (Figure 6G). To further address (ii) (Clementz et al., 2016; Yan and Ye, 2007), we reduced ensemble activity into three principal components using a VARIMAX factor rotation after P.C.A for each population imaged. We then carried out k-means clustering (clustering ensemble activations in P.C. space) for four representative datasets using k = 3 in order to depict i) the uniqueness of separate, observable ensemble states clusters in control mice and ii) the disruption thereof in disease models. Second, using all datasets, we carried out k-means repeatedly for each population from k = 2 to k = 15, repeating 100 times for each k to ensure the stability of the solutions, and quantifying the average within cluster distances (i.e., Euclidean distances), dividing by their decrease from the "1-cluster" solution (average distance from the overall mean; Figures 4B–4H). Next, we quantified the discrete first-derivative of this plot (Figures 4L–4N), estimating the degree to which added clusters parse the ensemble activation variance in P.C. space. Since large decreases in within-cluster distances were seen from k = 2 to k = 5, we compared these models across mice within experiments (SAL, KET, Df(16)A+/−) with one-way ANOVAs. (Note: "representative" datasets in Figures 2A, 2B, 3A–3H, 3L–3S, 6A–6L, S2A–S2D, S2I–S2L, S3, S5A, S5D, S6D–S6G, S7A, S7B, and S7D each originate from separate cell populations in order to better represent the breadth of the effects.)

Analysis of stimulus evoked activity

Δf values were averaged within trials (free of locomotion ± 3 s) from stimulus onset to offset and across trials of the same stimulus (approximately 15 trials per stimulus). Analyses focused on cells exhibiting significant stimulus evoked activity that is, cells for which the average stimulus evoked activity exceeds 1.67 standard deviation of the baseline for at least one stimulus orientation/direction (KET = 70%, SAL = 72%, Df(16)/WT = 75%; Hamm and Yuste, 2016). 1 SAL mouse and 1 KET mouse failed to show consistent stimulus elicited activity at week 1 and were excluded from this portion of the study. The orientation selectivity index (O.S.I), which estimates the degree to which a cell prefers lined visual stimuli of a particular angle or orientation, was calculated on average Δf responses (R) across 12 orientations (K; where θ is the angle of the stimulus direction, 0: 2pi radians) as

$$O.S.I = \left| \sum_k R_k \cdot \exp(2i\theta_k) \Big/ \sum_k R_k \right|.$$

This metric, akin to 1-circular variance, has been demonstrated to be stable and effective at detecting selectivity differences between populations (Mazurek et al., 2014). Although direction selectivity could be detected in some cells, it was sparse overall and weaker than O.S.I., in agreement with previous reports in V1 (Marshel et al., 2011), so analyses focused on O.S.I. Changes in overall O.S.I. for SAL/KET were tested with a 2-by-2 mixed ANOVA on individual cells with TREATMENT as the between subject variable and WEEK as the within subject variable. Significant interactions were followed up by a one way ANOVA.

Average responses across cells displaying orientation selectivity (O.S.I. of at least 0.1 given 30 trials per orientation per week; Mazurek et al., 2014) were plotted as a function of stimulus direction (x axis) on the same scale across conditions (Figures 6B, 6D, and 6F) by dividing responses by the response to their average "preferred" orientation at week 1 (SAL/KET) or the average "peak" across all neurons in DF16/WT (Lee et al., 2014). Cell response curves then were compared for SAL, KET, and DF16/WT with 2-by-12 MIXED ANOVAs with TREATMENT as a between subjects variable and WEEK as within subject variables. In KET, To understand the nature of the O.S.I. changes, additional analyses focused on cells visually identifiable and which showed visually driven activity in week 1 and 2 (n[SAL] = 45 cells, n = 4 mice; n[KET] = 62, n = 5 mice). For Figures S8A and S8C, the preferred angle of each cell was estimated similarly to the O.S.I, but instead of the absolute value, the imaginary component of the log transform of the above expression was calculated (i.e., computational preference).

For assessing noise correlations, we focused on visually active neurons with at least 0.1 O.S.I. (to ensure the reliability of the assessed "preferred orientation"). For each stimulus orientation, for each cell pair, we quantified the pearson correlation coefficient of average responses (stim-on mean minus baseline 1 s), and then averaged over different orientations. We then grouped pairs into shared preference (difference of computational preference ± 15 degrees), +/−45 (between 30 and 60 deg difference), and opposite (between 75 and 115 degrees). For SAL, KET, and Df(16)[+/−]/WT, we computed mixed ANOVAs on the proportion of significantly noise correlated neurons per mouse with ORIENTATION as a within-subjects factor and WEEK (or GROUP) as a between subjects factor (3X2). Next we applied these same statistical models to individual cell pairs.

Population level analyses of visually evoked responses utilized the same similarity metric as for ongoing activity analyses, but focused on average stimulus elicited responses across neurons on individual trials rather than "up-states." This step quantified whether directly evoked population-wide patterns of activity, without regard to single-cell orientation preferences or baseline levels of activity, were more similar across trials of the same stimulus type compared to different stimulus types. Similarity between all trials

was calculated on within trial averages (0-3.5 s post stim onset to account for offset induced activity), yielding a T by T matrix of similarity values where T = total trials (Figures 7B, 7D, 7F, and 7H). Next, bootstrapped similarity distributions described above were used to derive a mean and standard deviation of expected chance level population similarity for each mouse/neuronal-population studied. Individual trials (i.e., matrix cells in Figure 7B) were then rescored as "Z" scores for each trial, and these values were then averaged to yield (i) within-stimulus-type, (ii) cross-stimulus-type (30 and 60deg differences), and (iii) opposite stimulus type intertrial ensemble similarity (barplots in Figures 7M–7O). For SAL, KET, and Df(16)$^{+/-}$/WT, we then computed mixed ANOVAs on mouse-wise average population similarity z-scores with ORIENTATION difference as a within-subjects factor and WEEK (or GROUP) as a between/within subjects factor (3X2; within for KET/SAL).

For depiction of this effect on single trials (state-space plots in Figures 7I–7L), Δf values from −2 to 7 s post stimulus onset for all trials and all cells from one representative mouse from each condition were subjected to a PCA (cells as variables) with a VARIMAX rotation applied to the covariance matrix, thereby limiting and optimizing the resulting solution to a minimal number of components (usually 3-6, based on the screeplot). This enabled the n-dimensional network state space (n = number of neurons) in which similarity was computed to be plotted in 2 dimensions (principal component space). In Figure 7, single trials are plotted as continuous trajectories in time and color coded with regard to the stimulus the mouse saw on a given trial.

Acute ketamine and PV-suppression experiments

Calcium imaging data were processed and analyzed with the same methods and statistical comparisons as described above for chronic models. One-way ANOVAs were used for acute ketamine experiments (base versus sal versus KET) and two-way mixed ANOVAs were used for DREADD experiments (base VS CNO-control; base VS CNO-h4MD(Gi)), followed by one-way ANOVAs to follow-up on interactions.

Analysis of PV interneurons

For each interneuron we calculated change in florescence from baseline (2 s before each event), divided by the standard deviation of florescence during baseline across all time points (z-Δf/f). While this measure does not purely assess the absolute activity of PVs, it reliably indexes the signal to noise ratio of PV responses to visual stimuli and during spontaneous ensemble activations in the local network (Figure S7C) and results in PVs untreated mice conform with previously published properties of PVs (Hofer et al., 2011; Niell and Stryker, 2008). For statistical comparisons, cell responses were normalized within mice (see above). Visually evoked PV z-df/f scores were averaged within the 3 s of stimulus presentation and compared with 2-by-2 mixed ANOVAs with TREATMENT as the between subject variable and WEEK as the within subject variable. PV activity locked to statistically identified ensemble activations (above) was averaged within the first 2 s after peak network Δf and compared with 2-by-2 mixed ANOVAs with TREATMENT as the between subject variable and WEEK as the within subject variable.

ADDITIONAL RESOURCES

MOCO software for motion correction is available at http://www.columbia.edu/cu/biology/faculty/yuste/Methods/moco.zip.